Chapter 1

Introduction

Mechanical Ventilation (MV) and Ventilator-induced lung injury (VILI)

Acute respiratory distress syndrome (ARDS) and acute lung injury (ALI) are often fatal, inflammatory lung conditions that occur when a traumatic event i.e. pneumonia, shock, sepsis or massive aspiration leads to inflammation, increased pulmonary vascular permeability, and extravasation of fluid and inflammatory cells into the pulmonary interstitium and alveolar space (Rinaldo 1982). Approximately 150,000 Americans are affected each year and of those more than 40% die from ARDS (Seeman 2003). There are currently no specific therapies, and standard treatment is traditional mechanical ventilation (MV) with supplemental oxygen to provide adequate gas exchange and rest the respiratory muscles. The lung is a delicate structure and is highly sensitive to its mechanical environment, therefore abnormal physical forces, such as that from MV can often initiate or exacerbate any underlying lung injury, leading to the development of ventilator-induced lung injury (VILI) (Bezzant 1994, Parker 1993). VILI is a significant health risk for patients on MV, occurring in 5-15% of ventilated patients with an associated mortality rate of 34-60% (Cavanaugh 2002). Some of the symptoms characteristic of VILI include: increased pulmonary edema, impairment of the surfactant system, and disruption of the endothelium and alveolar epithelium. Loss of alveolar

compartmentalization subsequently can lead to the release of cytokines into the systemic circulation resulting in multiple system organ failure and death.

Mechanisms of VILI

VILI manifests itself primarily on the level of the alveolus (Figure 1.1a). Alveoli serve as the gas exchange units of the lung and are lined by the pulmonary alveolar epithelium- an integral part of the blood-air barrier. The alveolar epithelium consists of 2 morphologically distinct cell types: Type I cells are involved in gas exchange, and Type II cells are involved in the production and secretion of surfactant, a surface-active lipoprotein that serves to reduce surface tension at the air-liquid interface in alveoli (Dobbs 2002) (Figure 1.1b). The functions of the alveolar epithelium include maintaining a barrier to solvent and solute fluxes from the vasculature to the air space, synthesizing surfactant, allowing for rapid diffusion of gas for respiration, and in response to injury, facilitating the efficient clearance of alveolar edema (Crandall 1991).

VILI is characterized by the breakdown of the blood-gas barrier, which loses its size selectivity and allows a protein-rich fluid (alveolar edema) containing a large number of neutrophils to form in the alveolar air spaces. Injured lungs are generally divided into three regions: (1) regions where alveoli are collapsed at end expiration due to interstitial infiltration and open during inspiration, (2) regions where the air spaces are filled with exudates and not available for gas exchange, and (3) aerated normal lung, which can often be reduced to as less as 25% of normal lung volume in diseased lungs (Slutsky 1998). The inactivation, destruction, and decreased production of surfactant can increase the surface tension within the alveolus and also cause regions of closed alveoli.

Much research has been directed towards understanding the basis of VILI. Although the exact mechanisms underlying VILI remain unclear it has been proposed that its damaging effects are due to several factors: (1) lung overdistension in small airways and alveoli due to increased tidal volumes and compensation for nonrecruitable alveoli (volutrauma), (2) shear forces generated from the repetitive opening and closing of atelectatic regions filled with fluid (atelectrauma), and (3) mechanical stress-induced inflammation (biotrauma) (Bezzant 1994). Atelectasis is the incomplete expansion of clusters of alveoli that may result in partial or complete lung collapse. During MV, the repetitive collapse and re-expansion of alveoli that are deficient in surfactant can place injuriously high cyclic strain on the alveolar epithelial cells as well as generate high fluidic shear stresses as the alveoli walls adhere to each other when closed and then are forced apart during inflation. This becomes especially important when edema fluid floods the air space and during MV, alveoli undergo rapid and cyclic transitions from being small and flooded at end expiration to being large and air-flooded at end inspiration. This transition can generate high shear stresses at the alveolar surface while the edema fluid redistributes and the alveolar volume cyclically changes (Schumacker 2002). What can result is considerable cell disruption, rupture, and a massive inflammatory response.

Inflammatory response

VILI occurs when the ventilator settings required to sustain life can instead lead to a local inflammatory response in the lung (Figure 1.2). The response begins with an inflammatory insult, which can be either chemical (bacterial products) or mechanical (overdistension or injurious cyclic stretching of alveoli). Alveolar macrophages are

activated to release the early response cytokines (tumor necrosis factor (TNF)-α and Interleukin (IL)-1). Cytokines are small, soluble, regulatory proteins (8-80 kDa) produced by cells during the inflammatory process and function as messengers in cell to cell communication. They are active at picomolar and femtomolar concentrations and principally act in an autocrine or paracrine fashion to initiate, amplify, and perpetuate local and systemic inflammatory responses. TNF-α and IL-1 can effect a host of responses, one of which is stimulating the cells of the alveolar epithelium to secrete Interleukin (IL)-8, a potent neutrophil chemoattractant. Similarly mechanical signals that distress the alveolar epithelium can also directly lead to the release of IL-8 by the Type II alveolar epithelial cells. What follows is the process of neutrophil extravasation (along the IL-8 gradient) where neutrophils move from the blood vessels to the tissue interstitium. Once there, the activated neutrophils release reactive oxygen metabolites, proteolytic enzymes, and additional proinflammatory cytokines leading to alveolar macrophage proliferation, more interstitial lymphocyte infiltration, and destruction of the alveolar epithelium (Yamamoto 2002). The cycle of inflammation propagates into biotrauma where compartmentalization of the alveolar cytokines is lost and the cytokines released into the pulmonary circulation. The subsequent systemic inflammatory response can lead to multiple system organ failure and death (Tremblay 1997).

Ways to study VILI

Although MV with high tidal volumes has been implicated in VILI, what remains unknown are the specific mechanisms responsible for injury to the alveolar epithelium. The successful development of strategies to prevent VILI depends not only on understanding the physical responses of the alveolar epithelium to excessive strains, but

also the steps leading to the activation and regulation of the inflammatory response. Alveolar epithelial cells are believed to play a major role in the transduction of physical stimuli associated with MV. Recently there has been a growing interest in looking at the effects of mechanical strain on these cells, with the hypothesis that MV places injurious strains on the alveolar epithelium. As an important regulator of lung function, the degree of injury to the alveolar epithelium largely influences the prognosis and outcome of lung injury (Bilek 2003). Once the details of VILI are elucidated, therapies that not only limit mechanical injury to the lung but also constrain and modulate the inflammatory response can be developed.

Current methods to study the effects of VILI on the alveolar epithelium include: (1) animal, whole lung models, (2) dish cultures, and (3) cell stretching systems. The lung is an inherently heterogeneous, complex structure, making it difficult to isolate the specific consequences of particular mechanical stimuli in whole lung/animal models. Whole lung studies are also not ideal for examining lung inflation at the local or cellular levels, hence the use of *in vitro* cell culture models where the local environment can be controlled more readily. Traditional microscale *in vitro* assays generally involve the seeding of cells in static, flat multi-well plates and observing their behavior. Tissues in the body, however, are in a complex environment where cells are constantly exposed to dynamic fluidic surroundings. Stretching systems where mechanical strain is applied to cells cultured on a deformable substrate overcomes this limitation (Banes 1985, Wirtz 1990). These systems, however are low throughput and also macroscopic which is not ideal when recreating the alveolar microenvironment. Although these studies have provided valuable information about cellular behavior under mechanical strain, none

have considered the effects of cyclic strain on cells stretched at an air-liquid interface where cells are exposed to both deformations resulting from the solid substrate (cyclic strain) and from the fluid (high shear stresses). This raises the novel idea that it is the stretching of compromised, diseased fluid-filled lungs that is the main cause of VILI.

A solution that can provide the convenience and versatility of *in vitro* assays as well as provide an added degree of physiological relevance is to use microtechnology to recreate aspects of biological environments seen *in vivo*. Microfluidics and other microscale phenomena dominate at the cellular level making microtechnology crucial to the understanding of the cellular basis of life. These microtechnologies enable examination of complex behaviors of cells *in vitro* in ways not possible with macroscopic assays to provide insight into the intricacies of cellular biology.

The following chapters describe devices that take advantage of microtechnology and can potentially be used to study VILI. A fourth section describes a method of fabricating multigenerational branching networks for artificial vasculatures. In each case, the use of microfluidics is beneficial in recreating the small volumes found at the cellular level, facilitating the sampling of fluids, and allowing for the potential of integrating all components into one 'artificial alveoli' microchip. Future goals aim to study the hypothesis that increased mechanical stresses, namely the cyclic opening and reopening of alveolar units and fluidic shear stresses at the air-liquid interface, incurred during mechanical ventilation leads damage of the alveolar epithelial cells that is characteristic of VILI. It is this structural disruption along with an increase in alveolar-capillary permeability that contributes to the high mortality rate from VILI in mechanically ventilated patients.

1. Alveolar structures that expose cells to cyclic stretch

The stresses involved in cyclic stretching are implicated in initiating and propagating the inflammatory response during VILI. We have developed a device consisting of miniature cell stretching chambers with flexible bottom membranes that are deformed using the computer-controlled, piezoelectrically actuated pins of a Braille display. Morphologic changes of the cells, such as alignment, can be captured and analyzed efficiently.

2. Stretching alveolar epithelial cells at an air-liquid interface

In vivo the cells of the alveolar epithelium are exposed to stresses originating from the solid substrate as well as the fluidic environment. Current stretching devices do not allow for both of these factors. We have developed a system where cells can be stretched at an air-liquid interface to show greater levels of cellular injury.

3. Detection of cytokines released during inflammation

Elevated concentrations of inflammatory mediators are often found in the bronchial alveolar lavage fluid during acute lung injury. To measure levels of cytokines, we have developed a self-contained, connection-less, automated microfluidic immunoassay system where liquid flow is controlled using small mechanical actuators provided by the pins of a Braille display. The microfluidic system is capable of on-chip analysis of the biochemical responses of cells to cytokine exposure.

4. Fabrication of multigenerational branching networks

Recreating microfluidic systems that generate physiological flow patterns in terms of fluid velocities, resistances, and flow bifurcation patterns is critical for obtaining physiologically relevant results in tissue engineering and investigations in biomedical

fluidics problems. We have used a high-brightness diode-pumped Nd:YAG laser direct write method to fabricate multi-width multi-depth microchannel networks to generate biomimetic vasculatures.

The above microsystems have been used to show that some cells (endothelial cells and muscle cells) respond to cyclic stretch by aligning perpendicular to the direction of radial strain. Alveolar epithelial cells do not align, however even more interestingly they show increased amount of cell death when stretched with an air-liquid interface. This finding has significant implications to the study of VILI, by recreating situations found *in vivo* where cells are exposed to both deformations arising from fluid flow as well as from the solid mechanical environment.

Future development efforts will focus on integrating the above components in a continuous-flow microchip format. The combination of an on-chip cell culture dynamic microenvironment region integrated with a non-diluting immunoassay and nanoliter-scale liquid handling has the potential to create a truly advanced microfluidic cell-based bioassay system: an artificial alveoli where we are able to address the behavior of cells in a controlled mechanically active environment and further our understanding of the biomolecular and cellular effects of exposing the lung to such forces commonly encountered in patients with mechanical ventilation. The system can be used test the effect of ventilator settings and therapeutics on mechanical stress induced cell injury and determine the link between changes in volume to cytokine release and cell survival. Insights into the pathways from which excessive stretch is transduced into epithelial injury in VILI can profoundly alter the ventilator management of patients with ARDS or ALI.

(a)

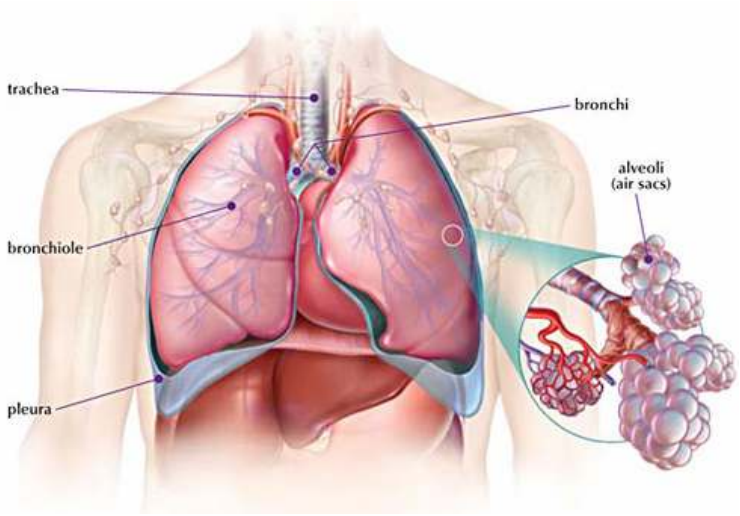

(b)

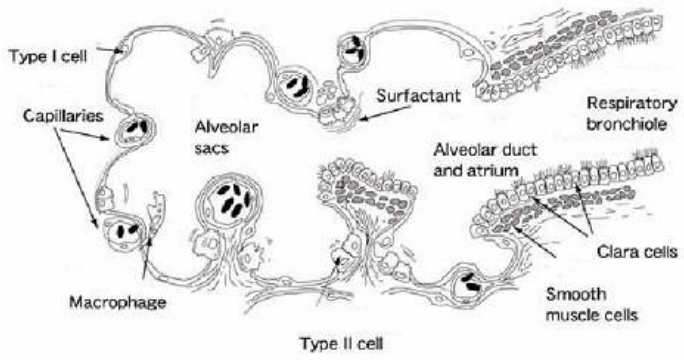

Figure 1.1: The anatomy of the lung. (a) Branching system of the lung ending in the alveoli (http://www.avastin.com). (b) Alveolar epithelium composed of Type I and II cells (http://www.lab.toho-u.ac.jp).

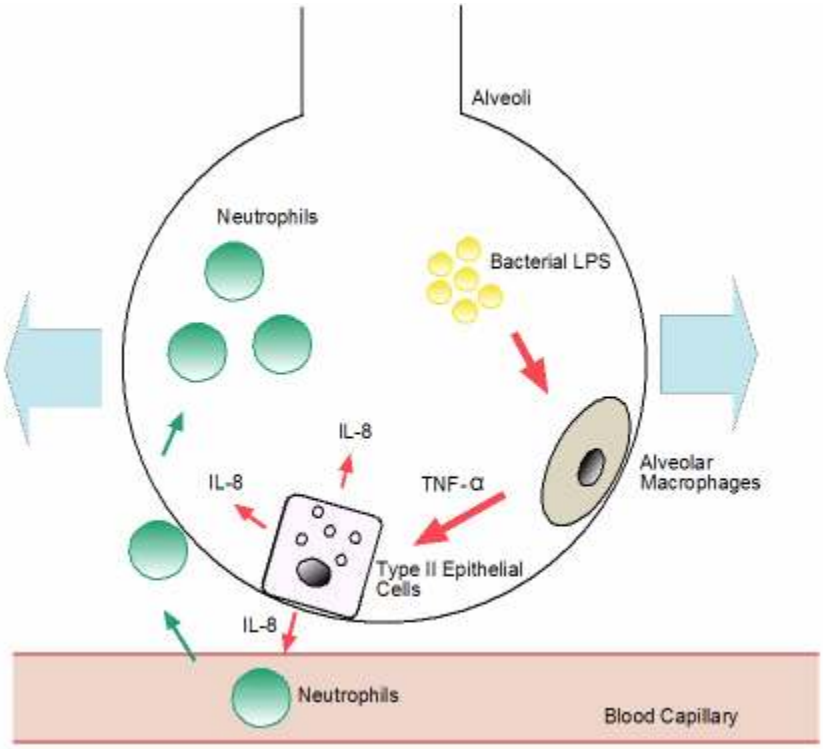

Figure 1.2: Cytokines released in the alveoli due to chemical stimulation or mechanical stretch. LPS: lipopolysaccharide, TNF-α: tumor necrosis factor-α, IL-8: interleukin-8.

References

Banes AJ, Gilbert J, Taylor D, Monbureau O. A new vacuum-operated stress-providing instrument that applies static or variable duration cyclic tension or compression to cell in vitro. J. Cell Sci. 1985; 75: 35-42.

Bezzant TB, Mortensen JD. Risks and hazards of mechanical ventilation: a collective review of published literature. Disease-a-Month. 1994;40: 581-640.

Bilek AM, Dee KC, Gaver III DP. Mechanisms of surface-tension-induced epithelial cell damage in a model of pulmonary airway reopening. J Appl Physiol 2003;94:770-783.

Cavanaugh KJ, Margulies SS. Measurement of stretch-induced loss of alveolar epithelial barrier integrity with a novel in vitro method. Am J Physiol Cell Physiol 2002; 283:1801-1808.

Crandall ED, Kim KJ. Alveolar epithelial barrier properties. In: The Lung: Scientific Foundations, edited by RG Crystal and JB West. New York: Raven, 1991, 273-287.

Dobbs LG, Gonzalez RF. Isolation and Culture of Pulmonary Alveolar Epithelial Type II Cells. Culture of Epithelial Cells, Second Addition. 2002 Wiley-Liss Inc. pp 277-301.

Parker JC, Hernandez LA, Peevy KJ. Mechanisms of ventilator-induced lung injury. Crit Care Med. 1993; 21: 131-143.

Rinaldo JE, Rogers RM. Adult respiratory-distress syndrome. N Engl J Med 1982;306:900-909.

Rodriguez-Caballero A, Garcia-Montero AC, Bueno C, Almeida J, Varro R, Chen R, Pandiella A, Orfao A. A new simple whole blood flow cytometry-based method for simultaneous identification of activated cells and quantitative evaluation of cytokines released during activation. Laboratory Invest. 2004; 84: 1387-1398.

Schumacker PT. Straining to understand mechanotransduction in the lung. Am J Physiol Lung Cell Mol Physiol 2002;282: L881-L882.

Seeman, B.T. (2003, May 15). Research dispute prompts debate over patient protection. Washington, DC: Newhouse News Service.

Slutsky AS, Tremblay LN. Multiple system organ failure; is mechanical ventilation a contributing factor? Am J Respir Crit Care Med. 1998;157: 1721-1725.

Tremblay L, Valenza F, Ribeiro J, Li J, Slutsky AS. Injurious ventilatory strategies increase cytokines and c-fos mRNA expression in an isolated rat lung model. J.Clin.Invest. 1997;99: 944-952.

Wirtz HRW, Dobbs LG. Calcium mobilization and exocytosis after one mechanical stretch of lung epithelial cells. Science. 1990; 250: 1266-1269.

Yamamoto, H, Teramoto H, Uetani K, Igawa K, Shimizu E. Cyclic stretch upregulates interleukin-8 and transforming growth factor-β1 production through a protein kinase C-dependent pathway in alveolar epithelial cells. Respirology. 2002; 7: 103-109.

Chapter 2

Individually Programmable Cell Stretching Microwell Arrays Actuated by a Braille Display

Cell culture systems are often static and are therefore nonphysiological. *In vivo*, many cells are exposed to dynamic surroundings that stimulate cellular responses in a process known as mechanotransduction. To recreate this environment, stretchable cell culture substrate systems have been developed, however these systems are limited by being macroscopic and low throughput. We have developed a device consisting of 24 miniature cell stretching chambers with flexible bottom membranes that are deformed using the computer-controlled, piezoelectrically actuated pins of a Braille display. We have also developed efficient image capture and analysis protocols to quantify morphological responses of the cells to applied strain. Human dermal microvascular endothelial cells (HDMECs) were found to show increasing degrees of alignment and elongation perpendicular to the radial strain in response to cyclic stretch at increasing frequencies of 0.2, 1, and 5 Hz, after 2, 4, and 12 hours. Mouse myogenic C2C12 cells were also found to align in response to the stretch, while A549 human lung adenocarcinoma epithelial cells did not respond to stretch.

2.1 Introduction

In the body, cells are continuously exposed to mechanical deformation originating from processes such as muscle movement, respiration, and the pulsatile nature of blood

flow. The ability of cells to sense and respond to mechanical strain is important in many tissues including the vasculature, lung alveoli, and skeletal muscle. The process by which cells convert mechanical signals into biochemical responses is known as mechanotranduction. Extracellular forces are transduced across the cell membrane to effect intracellular biochemical events such as proliferation, differentiation, and alignment. To study such events, cell culture systems designed to replicate *in vivo* situations where cells are exposed to mechanical stimuli, are useful to better represent physiological conditions.

To apply mechanical strain to cells *in vitro*, a variety of stretchable cell culture substrate systems have been developed. The majority of devices consist of cells cultured on a membrane (either a circular one held about its periphery, or a rectangular membrane held at the two ends) and stretch applied either multiaxially where there is a nonuniform strain through two axes (radial and circumferential) (Gilbert 1994), or uniaxially where there is a single axis of uniform tensile strain with a small magnitude of compression (Clark 2001). Multiaxial strain can be applied to circular membranes by injection of air or liquid into a chamber beneath the membrane (Brighton 1991, Williams 1992, Gorfien 1989) or direct displacement with an indentor (Hasegawa 1985, Vandenburgh 1988). Uniaxial strain is often applied by fixing one end of a rectangular membrane while the other end is attached to a motor-driven movable frame (Clark 2001, Naruse 1998).

These devices have demonstrated the value of *in vitro* stretching systems for a wide range of cellular studies. Existing cell stretching systems, however, are macroscopic and low throughput. Typically one cell type is exposed to one stretching condition per device. Commonly used devices have between 6 to 24 cell stretching wells

but expose all wells to the same stretching condition. What would enhance many *in vitro* studies and cellular screening assays would be the ability to test multiple conditions and cell types in parallel. Additionally, as the number of cellular samples that are exposed to different stretching conditions increases, the use of fewer cells and reagents, as well as the development of software algorithms to automate analysis of cellular responses to stretch in these array based systems would be required. A readily observed cellular response to mechanical stress is cell alignment. For example, upon cyclic stretching certain cells orient perpendicular to the direction of stretch including endothelial cells (Dartsch 1989, Iba 1991, Shirinsky 1989, Naruse 1998), fibroblasts (Danciu 2004), smooth muscle cells (Buck 1983, Mills 1997), cardiac myocytes (Terracio 1988), avian skeletal muscle cells (Vandenburgh 1988) and mesangial cells (Harris 1992).

Here, we describe a device with an array of miniature cell stretching chambers that enables efficient study of the effects of mechanical strain *in vitro* in a parallel manner amenable for higher throughput screening. The system uses microwells with flexible bottom membranes that are placed over the computer-controlled, piezoelectrically actuated pins of a refreshable Braille display (Figure 2.1a). Each pin is independently controlled according to a computer program to push against the flexible bottom membrane of the microwells and apply a cyclical radial strain to cells cultured on the membrane (Figure 2.1b). Computer control allows modification of parameters such as the frequency and duration of stretch, while an alteration in fabrication allows modification of the magnitude of stretch. Advantages to this device include the ability to create a microscale environment for cell culture and to run multiple experiments in parallel. The Braille device contains multiple independent pins, each of which can be

actuated at varying frequencies. Commercially available Braille displays typically have between 320 and 1536 pins. We constructed a custom setup (Futai 2006) that is more compact and has the potential to test up to 48 conditions with one display. We also developed image capture and automated image processing protocols to enable efficient analysis of morphological cellular responses across the multiple microwells. For biological validation we tested the response of three different cell types expected to behave differently in terms of cell alignment to mechanical stretch: (i) human dermal microvascular endothelial cells (Figure 2.1c,d) (HDMECs), (ii) A549 human lung adenocarcinoma epithelial cells, and (iii) mouse myogenic C2C12 cells.

2.2 Materials and Methods

Cells and growth media

Mouse myogenic cell line C2C12 cells and the human lung adenocarcinoma epithelial cell line A549 cells were obtained from American Tissue Type Culture Collection (ATCC, Manassas, VA). Growth medium for the C2C12 cells consisted of Dulbecco's Modified Eagle Medium (DMEM, Invitrogen, Calsbad, CA) supplemented with 10% fetal bovine serum (FBS, Invitrogen) and 1% antibiotic/antimycotic (Invitrogen). Growth media for the A549 cells consisted of Ham's F12K medium (ATCC) with 10% FBS (Invitrogen) and 1% antibiotic/antimycotic (Invitrogen). Human dermal microvascular endothelial cells (HDMECs) were obtained from Cambrex (Cambrex, East Rutherford, NJ) and cultured in endothelial growth medium-2 (EGM-2, Cambrex).

Cell stretching device

ANSYS Finite Element Analysis (FEA)

In order to estimate the strain generated on an elastomeric PDMS membrane top surface while the membrane is deformed by Braille pin movement, we performed simulations using finite element analysis (FEA) software, ANSYS 10.0 (ANSYS Inc., Southpointe, PA). To reduce the computational time, a 2-D model with an axis symmetric boundary condition was constructed (Figure 2.3a). The model was composed of a flat membrane and a curved Braille pin structure, where the pin structure was assumed to be rigid. Contact analysis was performed to simulate the interaction between the two objects. Contact and target elements, CONTA172 and TARGE169, were assigned on the Braille pin and the membrane bottom surface to simulate the surface-to-surface contact. The membrane was simulated using triangular 2-D elements, PLANE2. The axis symmetric boundary condition was assigned along the Y-axis, and one end of the membrane was assigned the fixed boundary condition. The displacement boundary condition, which was measured experimentally (Figure 2.3b), was assigned to the Braille pin. To simulate the large deformation of the PDMS membrane, non-linear, large deformation static analysis was performed. For all simulations, a Young's Modulus of 750 kPa and a Poisson's Ratio of 0.49 for the membrane were used.

Fabrication of chip and preparation for experiments

The three layer stretch chips were fabricated using the elastomer poly(dimethylsiloxane) (PDMS, Sylgard 184, Dow Corning, Midland, MI) and standard soft lithographic procedures (Whitesides 2001). Briefly, for the top layer, three large reservoirs of 1.5 cm diameter were punched into a cured slab of PDMS (10:1 prepolymer to curing agent) (dimensions: 7 cm x 2 cm x 0.5 cm height). For the middle layer, 24 microwells (1.7 mm diameter each) were punched into another PDMS slab of the same

dimensions. The bottom layer consisted of a 100 μm thick PDMS membrane formed by spin coating prepolymer onto a 4 inch diameter silanized silicon wafer and curing for 30 minutes in an 120°C oven. The top two layers were sealed using a PDMS glue mixture (2:3 PDMS prepolymer: toluene ratio) and curing in a 120°C oven for 20 minutes (Wu 2005). The bottom two layers were sealed irreversibly by treating both surfaces with plasma oxygen (SPI Supplies, West Chester, PA) for 30 seconds at 500 mtorr, and placing in a 120°C oven for 20 minutes post sealing.

After fabrication, the microwells were each filled with 10 μl of 50 μg/ml fibronectin (Invitrogen) solution in growth media and placed under UV sterilization for 30 minutes. The microwells were then washed twice with phosphate-buffered saline (PBS, Invitrogen) and filled, along with each large reservoir with 0.5 ml of cell culture media.

Culture of cells in PDMS microwells

At subconfluence, C2C12 and A549 cells were trypsinized from 100 mm diameter tissue culture plates. The trypsin (Invitrogen) was removed using centrifugation and the supernatant aspirated leaving a pellet of cells. After resuspending the cells in 8 ml of growth media, 100 μl of the cell solutions was pipetted into each large reservoir. HDMECs were grown in T-25 culture flasks and were washed and detached using 0.25% trypsin/EDTA (Invitrogen). After resuspension in growth media, the cells were seeded at a density of 100,000 cells/large reservoir. Each of the three cells types (ECs, A549, and C2C12 cells) were seeded into 4 separate stretching chips, one cell type per chip, for a total of 12 chips. All cells were left to attach overnight in a humidified 5% CO_2 incubator.

Cell stretching experiments

Braille display

The stretching was provided through the multiple, computer-controlled, piezoelectrically actuated pins of a refreshable Braille display. Each pin can be independently shifted upwards to push against the flexible bottom membranes of the PDMS microwells. Through a computer program, each pin can be programmed to move at a specified frequency. The PDMS chip was aligned over the Braille pin and held in place using a glass slide placed over the large reservoirs and a weight.

Stretching of cells

After incubating overnight, the chips were checked under a brightfield microscope to verify cell attachment and uniformity of cell coating on the bottom of the microwell. Three custom Braille displays were used for the experiment (one each for 2 hrs, 4 hrs, and 12 hrs). On each Braille display, three stretching chips (one per cell type) were carefully aligned over the pins. The remaining three chips were kept off the device as the controls. After covering the chips with a glass slide and a weight, everything was placed in the incubator. The computer program to begin pin movement was then started for all devices, this being time 0 hrs. Chips were removed at 2 hrs, 4 hrs, and 12 hrs for staining and imaging.

Fluorescence cell staining

Cells were stained using the LIVE/DEAD Viability/Cytotoxicity kit for mammalian cells (Invitrogen). Upon entering live cells, Calcein AM is converted into its green fluorescent form (ex/em 495 nm/515 nm) and is retained within the cell. 5 µl of 4mM Calcein AM in anhydrous DMSO (ATCC) was diluted into 495 µl of growth

media. 100 µl of this solution was then pipetted into each of the large reservoirs and allowed to incubate for 15 minutes. Afterwards, the liquid inside the large reservoirs was aspirated out and the wells imaged. At time 0, 2, 4, and 12 hours, one set of chips was removed from the Braille setup and stained for imaging.

All images were taken using Simple PCI imaging software program (Compix Inc. Cranberry Township, PA) connected to a CCD camera (Hamamatsu Orca-ER) mounted on an inverted phase contrast/fluorescence microscope (TE-300, Nikon, Tokyo) using the 4x and 10x objectives.

Quantification of alignment and elongation

Morphological changes were quantified using two variables; alignment direction and elongation ratio. All cells located in each microwell (on average 1000-2000 cells/microwell) were included in the analysis. Fluorescence images of cells stained with calcein AM, taken using the 4x objective (2 images per microwell) were processed using a semi-automated program created in ImageJ (NIH). The program was designed to process each grayscale image automatically by subtracting the background, thresholding to create a binary image where each pixel was either black or white, performing watershedding to better separate overlapping cells, fitting ellipses around each cell, and then removing background noise by ignoring ellipses too large or too small to represent a cell (Figure 2.2a,b,c). A data set was then generated including information such as: the number of ellipses in a microwell, and for each ellipse, the location of its centroid, the orientation angle, and the lengths along the major and minor axis. Each orientation angle was recalculated with respect to the center of the microwell as the center of the coordinate system (Figure 2.2d). Any angles over 90° were subtracted from 180° so that

all angles lay between 0 and 90°. For each cell, based upon its radial distance from the center of the microwell, cells located within 30% and outside of 90% of the radius were eliminated from the data set. This still represented over 70% of the total area within the well. Cumulative frequencies of cells located between 30 and 90% of the radius were then plotted versus orientation. Randomly oriented cells would result in a straight line of the plots while cells that orient perpendicular to stretch would result in a histogram skewed towards 90 degrees (Figure 2.2e). Cells with orientation angles between 80 and 90° were considered aligned and the percentage of aligned cells for each condition were calculated and plotted. Assuming the cell has an elliptical shape, the elongation ratio for the endothelial cells was calculated as the ratio of cell lengths along the major and minor axis.

Statistical Analysis

Results for the alignment analysis are presented as percentages of cells taken from duplicate wells. Results for the elongation measurements are presented as means ± standard deviation. Elongation data was compared using a two-sample t-test assuming equal variances with a $p < 0.05$ considered significant.

2.3 Results

Membrane thickness

Side view images of the Braille pin were taken under three conditions (Figure 2.3b): (i) without any load, the Braille pin extends a distance of 0.7 mm. (ii) When placed below a PDMS microwell with a bottom membrane of thickness 100 μm, the pin moves up 0.45 mm. (iii) For a thicker membrane (200 μm), the pin pushes upwards a distance of 0.3 mm. In each case, the Braille pin pushes up with a force (0.18 N initially,

and decreasing nonlinearly until maximum extension) against the stiffness of the membrane. Assuming a constant Young's Modulus, the deformation of the membrane is a result of its thickness. Figure 2.3c shows the results of the finite element analysis simulation for radial and tangential strains across the radius of the microwell.

Cell orientation angle and elongation ratio

Representative fluorescence images of unstretched cells (Figure 2.4a,c,e) and cells cyclically stretched at 5 Hz for 12 hrs (Figure 2.4b,d,f) are shown for the 3 cell types used in this study. Figure 2.5 shows the results obtained from the automated analysis of duplicate microwells for each condition and cell type. All cells within a microwell were analyzed for orientation angle relative to the center of the microwell and distance of its centroid from the center. Alignment was expected to occur perpendicular to the radial direction, which was the predominant strain direction. A cell angle between 80 and 90° corresponded to circumferential alignment. The percentage of cells that aligned were calculated and plotted versus each of the 5 conditions (Figure 2.5a). The elongation ratios (ratio of lengths along the major axis and minor axis of the cell) for the endothelial cells were also plotted (Figure 2.6).

2.4 Discussion

A dynamic environment for cells is often crucial to their growth, development, function, and even in the development of disease. It would therefore benefit many *in vitro* studies to recreate this biomechanical environment.

To study the response of cultured cells to strain, various stretchable cell culture substrate systems have been developed. Early methods used a vacuum to pull down an elastic circular membrane (Banes 1985). Currently the most widely used apparatus to

deliver controlled *in vitro* strain to cultured cells is the Flexercell Strain Unit (Flexcell Corp, McKeesport, PA). Adherent cells are cultured on flexible silicone membranes which are stretched over a loading post by applying negative vacuum pressure. Biaxial strain can be applied by using a circular loading post, while uniaxial strain is applied using an oblong-shaped post. The substrate can be elongated up to 30% and the computer-controlled vacuum can apply defined, controlled, static, or cyclic deformation in varying frequencies, amplitudes, and waveforms. Another version created by Flexercell is the strain unit (FX-2000) where circular silicone rubber surfaces form the bottom of 6-well culture plates. Application of a computer-controlled vacuum pressure deflects the surfaces downward (Banes 1985, Wirtz 1990). Limitations to this and other similar systems include the macroscopic dimensions and low throughput. The device described here overcomes these limitations with the capability of simultaneously applying radial cyclic stretch to 24 microwells at different frequencies.

The 64 pins of the Braille display are independently controlled with a computer program able to manipulate each pin's movement at a set frequency. Microwells with flexible PDMS bottom membranes are placed over the pin and deflected with the pin's upward movement. By combining a FEA simulation and experimental observations, the thickness of the PDMS membrane was selected to generate a biiaxial strain where the radial strain is significantly larger than the tangential (azimuthal) strain level. Previous studies have shown that endothelial cells undergo a 15% oscillation in its external diameter due to blood pulsation (Dobrin 1978), and alveolar epithelial cells experience mechanical strain levels of 8-12% normally and 17-22% in pathophysiological conditions due to respiratory cycles (Tschumperlin 2000). In the present study, in order to generate

radial strains greater than 15% on the membrane surface, the dimensions (microwell diameter and PDMS membrane thickness) of the chip was selected to provide a high radial/tangential strain ratio when stretched. As seen in Figure 2.3c, a 100 μm thick membrane with a microwell of 1.7 mm diameter, when stretched by the pin can provide 20-25% maximal stretch in the radial direction while the tangential stress is kept below 12%. As shown in Figure 2.3c, the radial strain is dominant over the tangential strain at each position in the microwell except for in the center where the strain is biaxial. Maximum radial strain occurs in a concentric circle halfway to the radius of the microwell and drops off near the outer edges. Under these conditions, the increase in surface area in the stretched state compared to the relaxed state is 17.2% over the total surface of the microwell and 20.9% between 30 and 90% of the radius. For the thicker membrane (200 μm), simulation results show nearly equal levels of radial and tangential strain throughout the microwell (Figure 2.3c).

Although several stretch devices, such as the Flexercell strain unit, have created configurations to generate a uniform biaxial strain profile (equivalent radial and circumferential strain) (Schaffer 1994), nonuniform strain fields such as that exhibited by the current stretch device may be more physiological. In the body, strain values can be markedly nonuniform and can depend upon factors such as the surrounding tissue, distending force, or internal pressure. For example, *in vivo* alveolar expansion due to respiratory cycles has been found to be nonuniform. When stretched to 82% of total lung capacity (TLC), the alveolar perimeter is distended by 14%, however within the alveolus, certain areas distended as little as 5% or as much as 25% of initial (Perlman 2007). Endothelial cells are subjected to cyclical strain due to expansion and contraction of the

blood vessel. Throughout the vasculature, the level of local strain induced by the blood pressure waveform acting on the vessel wall compliance is largely nonuniform (Carosi 1992). During normal circulation, the internal circumference of large arteries such as the pulmonary artery can vary between 2 and 18% (Dobrin 1978). Similarly, in the complex structures that comprise muscle, the distribution of strain can vary depending on many factors, such as whether the muscle is inactive or contracting. The presence of active and passive motor units along the muscle length can also cause variable force resulting in nonuniform strain values (Finni 2003). Because the readout of interest for the purposes of this work was cell alignment, the membrane and well dimensions were designed to generate strain fields where the radial strain was ~10% higher than the tangential strain over ~70% of the area (Figure 2.3c). Depending on the specific needs, the strain fields can be further modified by adjusting the well shape, membrane thickness and/or the shape of the pin.

All cell types were seeded at a density averaging approximately 1000 cells/microwell. Higher cell densities were avoided to prevent the formation of large aggregates of cells, which were difficult to separate using the automatic analysis program. With endothelial cells, too low a cell density caused many cells to die (data not shown). Endothelial cells and C2C12 cells, when cyclically stretched, have been shown to align perpendicular to the radial strain (Takemasa 1997, Moretti 2004, Dartsch 1989, Sipkema 2003, Naruse 1998, Birukov 2003, Iba 1991, Hornberger 2005, Akimoto 2001). In this case, the cells would be expected to align in a concentric pattern around the center of the microwell.

Each microwell contained a range of 500-2000 cells and we performed experiments with hundreds of microwells. Thus, it became prudent to perform morphological analysis using automated processing. A plugin using ImageJ (NIH) analysis software was developed which allowed us to take each image, convert all cells into ellipses, then compute the angle of orientation, lengths along the major and minor axis, and location of the cell. Cells located at the center and edges of the microwell (less than 30% and greater than 90% of the radius) were eliminated from the data set. To justify this step, the percentage of cells aligned in radial segments of 10% (between 0-10%, 10-20%, etc) was calculated and plotted versus the simulated difference in radial and tangential strains. One of the areas where the most cells aligned occurred between 90-100% of the radius (Figure 2.7). This was a region where the cells may have aligned due to their proximity to the edge rather than as a physiological response to stretching. In this region, the radial strain is also negative, hence the cells were being compressed rather than stretched (Figure 2.3c). Cells within 30% of the radius were also eliminated because of smaller difference in tangential to radial strain as well as to account for wells where the Braille pin is not centered exactly under the center of the microwell. Previous studies, using a circular substrate for cell culture, have analyzed cell alignment by either choosing random areas on the membrane, or by focusing on three main regions (the center, middle, and periphery) (Standley 2002). The automated processing described here, allows one to analyze all cells in the microwell and is time efficient, eliminates user bias, and can be easily adapted for a variety of other measurements. Image capture is also done quickly, with 2 images taken using the 4x objective per microwell. While ideal for analyzing EC and A549 cells, this analysis was limited in analyzing the C2C12 cells

due to their shape and density. For the C2C12 cells it was necessary to manually inspect each ellipse image and if necessary, separate cells in areas with a large overlap of cells by manually drawing fine lines to separate individual cells.

In the present experiments, the alignment of cells perpendicular to the radial strain can be discussed in view of physiological conditions. Both endothelial cells and C2C12 cells, are known to align when exposed to mechanical strain *in vivo.*

In vivo, endothelial cells appear spindle-like and align longitudinally on the luminal surface of a blood vessel. They are exposed continuously to mechanical stimulation such as fluid shear stress from the circulating blood, but also periodic stretching and relaxing caused by blood pulsation. The pulsatile nature of this blood flow along with its pressure waveform acts on the compliance of the arterial wall to produce circumferential stretching of the wall. In response, endothelial cells align to form the most efficient functional configuration, orienting roughly parallel to the longitudinal axis (Standley 2002). Previous studies have shown that ECs subject to cyclical deformation ranging from 10 to 20% elongate and reorient perpendicular to the stretch direction (Moretti 2004, Dartsch 1989, Sipkema 2003, Naruse 1998, Birukov 2003, Iba 1991). In our device, endothelial cells were shown to align in response to radial stretch, with the greatest percentage of aligned cells (31.1%) occurring at a pin frequency of 5 Hz after 12 hrs versus the control unstretched cells (10.8%) (Figure 2.5a). The EC cells also elongated in response to both stretch frequency and time (Figure 2.5b) with the greatest elongation change occurring at 12 hours after stretch at 5Hz (1.86 ± 0.64 versus the unstretched 1.65 ± 0.47, $P < 0.05$).

Mechanical stimuli are believed to also significantly influence skeletal muscle which experiences several types of loads *in vivo* such as longitudinal load during developmental bone growth and cyclic loading during exercise and movement (Collingsworth 2000). Akimoto et al. found that after growing C2C12 cells in the Flexcell system and exposing them to 20% cyclic stretch for 24 hrs, the cells oriented at an oblique angle on either side of the stretching plane (Akimoto 2001). In our studies, C2C12 cells aligned perpendicular to the radial direction (Figure 2.5a), with the greatest percentage of aligned cells (26.0% versus the control at 11.3%) occurring after 12 hrs of stretch at 5 Hz. The data, in this case, is not as clear as the EC cells due to the difficulty in automatically analyzing the orientation angles. C2C12 cells have a spindle-like morphology and cytoplasmic extensions, which make it difficult to fit ellipses around each cell and had to be manually separated.

Physical forces also play an important role in regulating the structure, function, and metabolism of the lung (Clark 2001). The alveolar epithelium, comprised of Type I and Type II cells, lines the alveolar air sacs of the lung and experiences cyclical mechanical deformation due to respiratory cycles. Type II alveolar epithelial cells that cover 3-7% of the alveolar surface, are small, cuboidal cells (diameter 10 μm) predominantly located in the corners of alveoli. *In vivo* Type II cells serve as the progenitor of the Type I cells, transdifferentiating into the squamous Type I cells (Crapo 1983). The A549 cell line, representative of the Type II cells, maintains a similar cuboidal shape in culture, however does not undergo morphological changes to differentiate into the elongated Type I-like cells (Foster 1998). In response to mechanical stimulation the A549 cell line is thus not expected to elongate or align. Our results show

that, in contrast to endothelial cells, the A549 alveolar epithelial cells were shown to have little response morphologically to cyclic stretch. As shown in Figure 2.5, A549 cells had little change in orientation angle (10.8% cells aligned in control versus 13.8% after stretching at 5Hz for 12 hrs) due to stretching conditions.

2.5 Conclusions

The system described here is a fast and easy-to-fabricate device to expose cells to cyclical stretch at different frequencies. Endothelial and C2C12 cells align perpendicularly in response to the radial strain. From the simulation results, it is shown that the radial and tangential strain field across the surface of the microwell is nonuniform but adjustable depending on specific needs. The thickness of the membrane is a significant factor in the strains generated. The well size and shape can also be manipulated to alter strain fields. Another possibility to manipulate the strain fields that has not been explored here is to manipulate the shape of the Braille pin. The pin can also be shaped to have minimal contact with the membrane, for example with a pointed end. Future work will focus on increasing the throughput of the device, by the addition of more microwells. Although this paper focused mainly on cell alignment, the present device has the potential to be also used to study other effects of cyclic stretch on cells such as the disruption of the basement membrane of epithelial cells leading to increased barrier permeability and cell death (Tschumperlin 2000), cytoskeletal rearrangements like actin remodeling (Dartsch 1989), activation of changes in gene expression (Takemasa 1997, Birukov 2003, Chien 1998), and the release of factors such as cytokines and growth factors (Carosi 1992). The device is also amenable to the study of other cell types and their responses to strain. With its ease of fabrication and quick image capture and

analysis protocols, this cell stretching device is ideal for studying the responses of cultured cells to mechanical strain and will benefit *in vitro* studies of mechanotransduction.

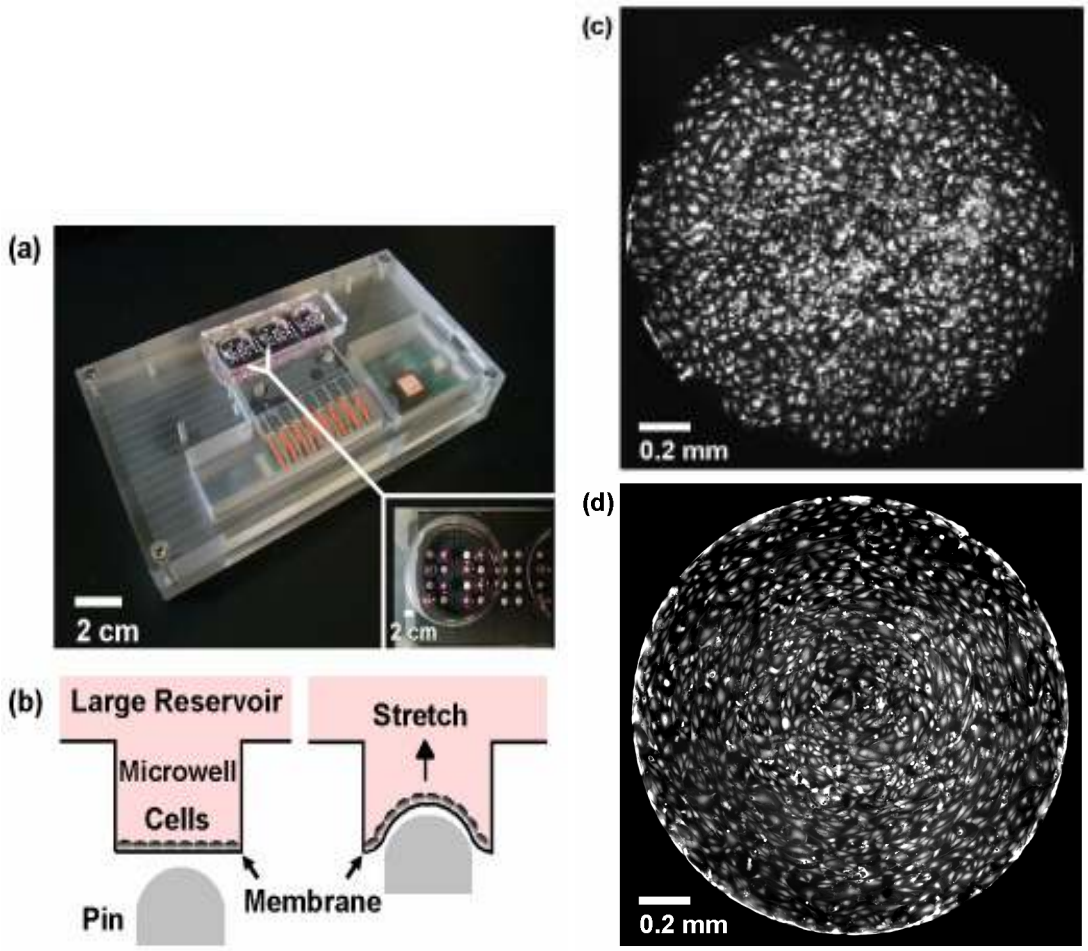

Figure 2.1: (a) PDMS device with 24 millimeter-sized cell stretching wells placed over a pin actuator array. The 24 microwells are divided into 3 larger reservoirs with 8 microwells each (inset). (b) Schematic figure of how cells are cultured on flexible membranes at the bottom of the microwells. When the pin moves upwards, it deforms the membrane and applies strain to the cells. Fluorescence micrographs of endothelial cells cultured in the wells, unstretched (c) and after application of cyclic stretch at 5 Hz for 12 hours (d). The diameter of the microwells is 1.7 mm.

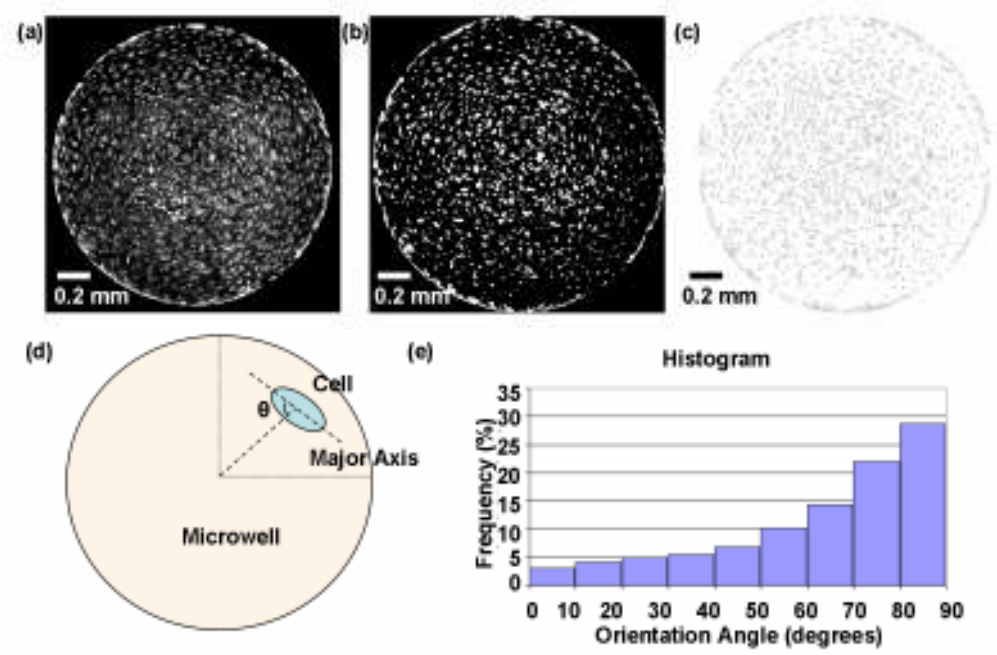

Figure 2.2: Automated image analysis using ImageJ (NIH). (a) Original fluorescence micrograph of endothelial cells subjected to stretch at 5 Hz for 12 hrs and stained with calcein AM. During processing, images were thresholded to create a binary black and white image (b) and ellipses were automatically fitted around each cell (c). The orientation angle (θ) was calculated as the angle between the major axis of the ellipse and a line extending from the center of the well to the ellipse centroid (d). (e) Alignment histogram with the distribution of cell orientation angles.

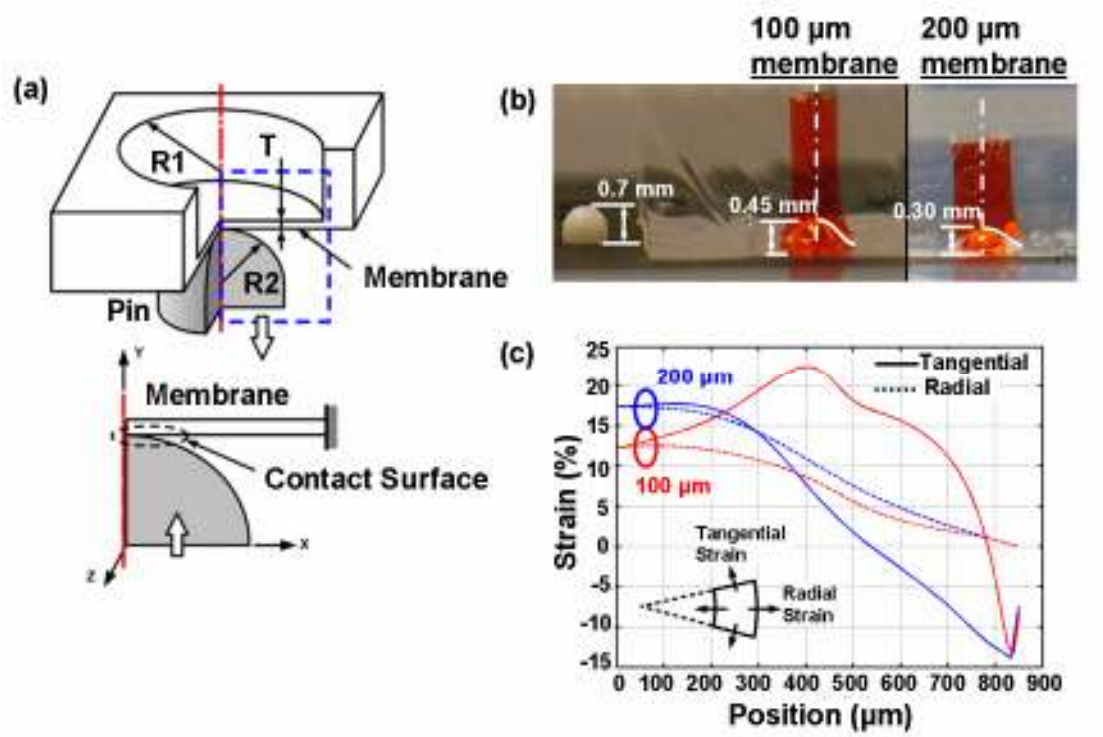

Figure 2.3: ANSYS Finite Element Analysis simulation of membrane stretching. (a) 2-D model for pin (radius R2) contacting a microwell (radius R1) with a flexible bottom membrane (thickness T). (b) Experimental results of Braille pin pushing upwards with no load (far left), pushing against PDMS membranes of thickness 100 µm (center) and 200 µm (far right). (c) Simulated radial and tangential strains on membranes of different thicknesses.

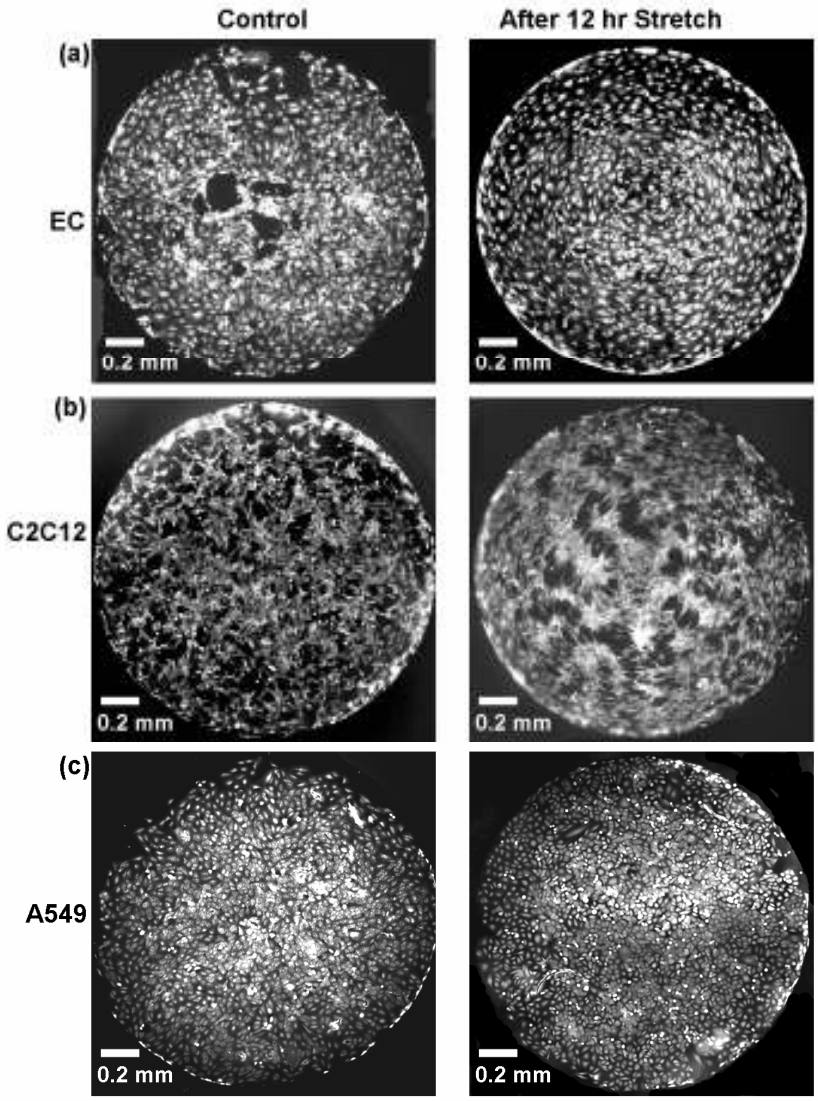

Figure 2.4: Fluorescent images of cells stained with Calcein AM before stretch (left column) and after cyclically stretching at 5Hz for 12 hrs (right column). Three cell types (a) Endothelial cells, (b) C2C12 myoblast cells, and (c) A549 alveolar epithelial cells were used.

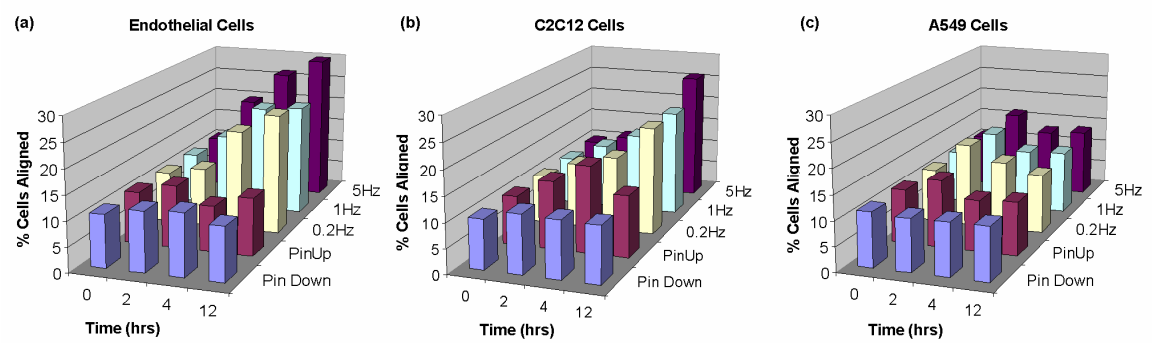

Figure 2.5: Percentage of cells within 30 and 90% of the radius with orientation angles between 80-90°, with 90° considered perfect alignment. Data shown as totals between duplicates for endothelial cells (a), C2C12 cells (b), and A549 cells (c).

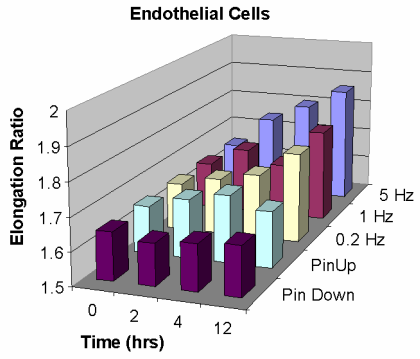

Figure 2.6: Average elongation ratio for endothelial cells for each condition. Elongation ratio is defined as the length of the cell along the major axis divided by the length along the minor axis.

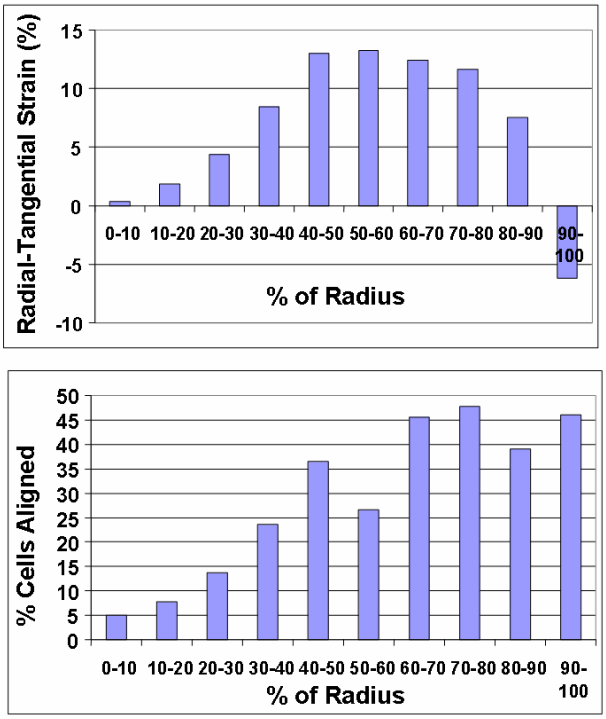

Figure 2.7**:** Top: From simulation results, the difference between radial and tangential strain (%) across the membrane. Bottom: For one experiment of endothelial cells stretched at 5 Hz for 12 hrs, the percentage of cells aligned (between 80-90°) for each radial segment.

2.6 References

Akimoto T, Ushida T, Miyaki S, Tateishi T, Fukubayashi. Mechanical stretch is a down-regulatory signal for differentiation of C2C12 myogenic cells. Materials Sci and Eng C; 2001. 17;75-78.

Banes AJ, Gilbert J, Taylor D, Monbureau O. A new vacuum-operated stress-providing instrument that applies static or variable duration cyclic tension or compression to cell in vitro. J. Cell. Sci 1985;75: 35-42.

Birukov KG, Jacobsen JR, Flores AA, Ye SQ, Birukova AA, Verin AD, Garcia JGN. Magnitude-dependent regulation of pulmonary endothelial cell barrier function by cyclic stretch. Am J Physiol Lung Cell Mol Physiol. 2003;285:L785-L797.

Birukov KG, Shirinsky VP, Stepanova OV, Tkachuk VA, Hahn AWA, Resink TJ, Smirnov VN. Stretch affects phenotype and proliferation of vascular smooth muscle cells. Molecular and Cellular Biochemistry 2003;36:653-659.

Brighton CT, Strafford B, Gross SB, Leatherwood DF, Williams JL, Pollack SR. The proliferative and synthetic response of isolated calvarial bone cells of rats to cyclic biaxial mechanical strain. J Bone Joint Surg [Am] 1991; 73:320-331.

Buck RC. Behavior of vascular smooth muscle cells during repeated stretching of the substratum in vitro. Atherosclerosis 1983;46:217-223.

Carosi JA, Eskin SG, McIntire LV. Cyclical strain effects on production of vasoactive materials in cultured endothelial cells. J. of Cellular Phyiol. 1992;151:29-36.

Chien S, Li S, Shyy YJ. Effects of mechanical forces on signal transduction and gene expression in endothelial cells. Hypertension. 1998;31:162-169.

Clark CB, Burkholder TJ, Frangos JA. Uniaxial strain system to investigate strain rate regulation in vitro. Rev Sci Instrum 2001; 72: 2415-2423.

Collingsworth AM, Torgan CE, Nagda SN, Rajalingam RJ, Kraus WE, Truskey GA. Orientation and length of mammalian skeletal myocytes in response to a unidirectional stretch. Cell Tissue Res 2000; 302: 243-251.

Crapo JD, Young SL, Fram EK, Pinkerton KE, Barry BE, Crapo RO. Morphometric characteristics of cells in the alveolar region of mammalian lungs. Am Rev Respir Dis. 1983;128:S42-S46.

Dartsch PC, Betz E. Response of cultured endothelial cells to mechanical stimulation. Basic Res Cardiol. 1989; 84:268-281.

Danciu TE, Gagari E, Adam RM, Damoulis PD, Freeman MR. Mechanical strain delivers anti-apoptotic and proliferative signals to gingival fibroblasts. J Dent Res 2004;83:596-601.

Dobrin PB. Mechanical Properties of arteries. Physiol Rev 1978; 58: 397-460.

Finni T, Hodgson JA, Lai AM, Edgerton VR, Sinha S. Nonuniform strain of human soleus aponeurosis-tendon complex during submaximal voluntary contractions in vivo. J Appl Physiol 2003;95:829-837.

Foster KA, Oster CG, Mayer MM, Avery ML, Audus KL. Characterization of the A549 cell line as a Type II pulmonary epithelial cell model for drug metabolism. Exp Cell Res 1998;243:359-366.

Futai N, Gu W, Song JW, Takayama S. Handheld recirculation system and customized media for microfluidic cell culture. Lab Chip 2006;6:149-154.

Gilbert JA, Weinhold PS, Banes AJ, Link GW, Jones GL. Strain profiles for circular cell culture plates containing flexible surfaces employed to mechanically deform cells *in vitro*. J. Biomechanics: 1994; 27, 1169-1177.

Gorfien SF, Winston FK, Thibault LE, Macarak EJ. Effects of biaxial deformation on pulmonary artery endothelial cells. J Cell Physiol 1989; 139:492-500.

Harris RC, Haralson MA, Badr KF. Continuous stretch-relaxation in culture alters rat mesangial cell morphology, growth characteristics, and metabolic activity. Lab Invest. 1992; 66: 548-554.

Hasegawa S, Sato S, Saito S, Suzuki Y, Brunette DM. Mechanical stretching increases the number of cultured bone cells synthesizing DNA and alters their pattern of protein synthesis. Calcif Tissue Int 1985; 37:431-436.

Hornberger TA, Armstrong DD, Koh TJ, Burkholder TJ, Esser KA. Intracellular signaling specificity in response to uniaxial vs. multiaxial stretch: implications for mechanotransduction. Am J Physiol Cell Physiol 2005;288:185-194.

Iba T, Maitz S, Furbert T, Rosales O, Widmann MD, Spillane B, Shin T, Sonoda T, Sumpio BE. Effect of cyclic stretch on endothelial cells from different vascular beds. Circ Shock 1991;35:193-198.

Mills IC, Cohen R, Khurram K, Guangdi L, Shin T, Du W, Sumpio BE. Strain activation of bovine aortic smooth muscle cell proliferation and alignment: study of strain dependency and the role of protein kinase A and C signaling pathways. J. Cell Physiol 1997; 170: 228-234.

Moretti M, Prina-Mello A, Reid AJ, Barron V, Prendergast PJ. Endothelial cell alignment on cyclically-stretched silicone surfaces. Journal of Materials Science 2004; 15:1159-1164.

Naruse K, Yamada T, Sokabe M. Involvement of SA channels in orienting response of cultured endothelial cells to cyclic stretch. Am J. Phsiol 1998; 274:H1532-H1538.

Perlman CE, Battacharya J. Alveolar expansion imaged by optical sectioning microscopy. J Appl Physiol 2007;103:1037-1044.

Schaffer JL, Rizen M, L'Italien GJ, Benbrahim A, Megerman J, Gerstenfeld LC, Gray ML. Device for the application of a dynamic biaxially uniform and isotropic strain to a flexible cell culture membrane. J. of Orthopaedic Research 1994;12: 709-719.

Shirinsky VP, Antonov AS, Birukov KG, Sobolevsky AV, Romanov YA, Kabaeva NV, Antonova GN, Smirnov VN. Mechano-chemical control of human endothelium orientation and size. J Cell Biol. 1989;109:331-339.

Sipkema P, van der Linden PJW, Westerhof N, Yin FCP. Effect of cyclic axial stretch of rat arteries on endothelial cytoskeletal morphology and vascular reactivity. Journal of Biomechanics 2003; 36:653-659.

Standley PR, Camaratta A, Nolan BP, Purgason CT, Stanley MA. Cyclic stretch induces vascular smooth muscle cell alignment via NO signaling. Am J Physiol Heart Circ Physiol 2002;283:H1907-H1914.

Takemasa T, Sugimoto K, Yamashita K. Amplitude-dependent stress fiber reorientation in early response to cyclic strain. Experimental Cell Res. 1997;230:407-410.

Terracio L, Miller B, Borg TK. Effects of cyclic mechanical stimulation of the cellular components of the heart: In vitro. In Vitro Cell Dev Biol. 1988; 24: 53-58.

Tschumperlin DJ, Oswari J, Margulies SS. Deformation-induced injury of alveolar epithelial cells. Am J Respir Crit Care Med. 2000; 162: 357-362.

Vandenburgh HH. Computerized mechanical cell stimulator for tissue culture: effects on skeletal muscle organogenesis. In vitro cell dev Biol 1988; 24: 609-619.

Whitesides GM, Ostuni E, Takayama S, Jiang XY, Ingber DE. Soft lithography in biology and biochemistry. Annu. Rev. Biomed. Eng., 2001; 3: 335-373.

Williams JL, Chen JH, Belloti DM. Strain fields on cell stressing devices employing clamped circular elastic diaphragms as substrates. J Biomech Eng 1992; 114:377-384.

Wirtz HR., Dobbs LG. Calcium mobilization and exocytosis after one mechanical stretch of lung epithelial cells. Science 1990; 250: 1266-1269.

Wu H, Huang B, Zare RN. Construction of microfluidic chips using polydimethylsiloxane for adhesive bonding. Lab on a Chip 2005; 5: 1393-1398

Chapter 3

Air-liquid Interface Causes Greater Damage to Alveolar Epithelial Cells During Stretching

Ventilator-induced lung injury (VILI) is a significant concern for patients placed on mechanical ventilators. VILI involves damage to the alveolar epithelium although the exact mechanisms leading to injury remain unknown. Previous studies have focused on the isolated effects of cyclic stretch or fluid mechanical stresses on the alveolar epithelium as the cause of VILI. We have shown that alveolar epithelial cells exposed to both types of stresses by stretching with an air-liquid interface show greater degrees of injury than with either stimulus alone. Changes in cellular viability can be visualized under physiologically relevant solid and fluidic deformations.

3.1 Introduction

The standard treatment for patients suffering from acute respiratory distress syndrome (ARDS) is mechanical ventilation (MV) to provide adequate gas exchange and rest the respiratory muscles. In some cases, however, the ventilator settings required to sustain life can instead initiate or exacerbate the underlying lung injury in what is termed ventilator-induced lung injury (VILI). VILI is characterized by the breakdown of the blood-gas barrier, which loses its size selectivity and allows a protein-rich edema to form. The alveolar air spaces are flooded with proteinaceous exudates that contain large numbers of neutrophils. Also present is the dysfunction or deficiency of surfactant, a thin

liquid film that lines the inner alveolar surface and acts to stabilize the alveoli by lowering the surface tension. The prevention or attenuation of VILI requires knowledge of the sequence of events that begins with a mechanical insult to the lung and ends in considerable cell death within the alveolar epithelium.

It has been proposed that the excessive mechanical stretch during MV is a contributing factor in the pathogenesis of VILI. Although the exact mechanisms underlying VILI remain unknown, one of the theories behind VILI suggest that structural disruption of the alveolar epithelium is due to shear forces generated from the repetitive opening and closing of atelectatic regions filled with fluid (Bezzant 1994). Atelectasis is the incomplete expansion of clusters of alveoli that may result in partial or complete lung collapse. During MV, the repetitive collapse and re-expansion of alveoli that are deficient in surfactant can place injuriously high cyclic strains on the alveolar epithelial cells. Similarly the collapse and reopening of alveoli can create large fluid mechanical stresses on the cells as the alveolar walls adhere to each other through the thin layer of surfactant when the alveoli are closed and then are forced apart during inflation. This becomes especially important when edema fluid floods the air space and during MV, alveoli undergo rapid and cyclic transitions from being small and flooded at end expiration to being large and air-filled at end inspiration. This transition can generate both high substrate mechanical and fluid mechanical stresses at the alveolar surface as the edema fluid redistributes and the alveolar volume cyclically changes (Schumacker 2002).

To examine the ways in which increased mechanical forces associated with MV can induce or aggravate acute lung injury, previous studies have focused on the effect of varying degrees of strain on cells cultured on deformable substrates. Tschumperlin et al.

have shown increasing levels of injury to alveolar epithelial cells with increasing strain magnitude and duration (Tschumperlin 1998). Others have focused on the effects of fluid mechanical stresses on epithelial cells by propagating an air bubble down a rigid tube lined with cells (Bilek 2003, Huh 2007). Although these studies have provided valuable information about cellular behavior under mechanical strain, none have considered the effects of cyclic strain on cells stretched using an air-liquid interface where cells are exposed to both deformations resulting from the solid substrate (cyclic strain) and from the movement of fluid (fluid mechanical stresses). This raises the novel idea that it is the movement of the air-liquid interface in compromised, diseased fluid-filled lungs that is the most damaging aspect of VILI.

We have developed an *in vitro* system that allows cultured cells to be stretched using an air-liquid interface to recreate the injurious environment found within alveoli during MV. We focused on an immediately observable characteristic of cellular injury, namely cell death inflicted by mechanical forces. Changes in cellular viability are observable after exposure to physiologically relevant solid and fluidic deformations.

3.2 Materials and Methods

Cells and growth media

A549 Type II human lung adenocarcinoma epithelial cells were obtained from American Tissue Type Culture Collection (ATCC, Manassas, VA). Growth media consisted of F-12K medium (ATCC) supplemented with 10% fetal bovine serum (FBS, Invitrogen, Calsbad, CA) and 1% antibiotic/antimycotic (Invitrogen). Fibronectin was also obtained from Invitrogen and reconstituted in distilled water. Survanta (Abbott

Laboratories, North Chicago, IL) was obtained from the VA hospital at the University of Michigan and diluted in serum-free culture media prior to use.

Fabrication of chip and preparation for experiments

The stretching wells were fabricated using the elastomer poly(dimethylsiloxane) (PDMS, Sylgard 184, Dow Corning, Midland, MI) and standard soft lithographic procedures (Whitesides 2001). Briefly, for the layer with wells, circular reservoirs (6 mm diameter) were punched into a cured slab of PDMS (10:1 prepolymer to curing agent) (dimensions: 2 cm x 2 cm x 0.5 cm height) using a biopsy punch. A 100 μm thick PDMS membrane was formed by spin coating prepolymer (370 rpm for 240 seconds) onto a 4 inch diameter silanized silicon wafer and curing for 30 minutes in a 120°C oven. The two layers were sealed irreversibly by treating both surfaces with plasma oxygen (10W, SPI Supplies, West Chester, PA) for 30 seconds at 500 mtorr, and placing in a 120°C oven for 5 minutes post sealing.

After removal from the oven, the wells were each filled with 50 μl of a 50 μg/ml fibronectin (Invitrogen) solution diluted in serum-free growth media and placed under UV sterilization for 30 minutes. The wells were then washed twice with phosphate-buffered saline (PBS, Invitrogen) and filled with 30 μl of growth media prior to cell seeding.

Culture of cells in PDMS wells

At subconfluence, A549 cells were trypsinized from 100 mm diameter tissue culture plates. The trypsin (Invitrogen) was removed using centrifugation and the supernatant aspirated leaving a pellet of cells. After resuspending the cells in 6 ml of growth media, 30 μl of the cell suspension was pipetted into each well. The cells were

left to attach overnight in a humidified 5% CO2 incubator. After 24 hours, the media in each of the wells was replaced with fresh media. 48 hours post seeding, the wells were checked under a brightfield microscope to verify uniformity of cell coating on the bottom of the microwell before starting experiments.

Stretching experiments

Linear actuator

In order to generate a linear actuation motion to stretch the PDMS membrane and attached cells, a setup (Figure 3.1a) using a voice coil motor (NCC01-04-001-1X, H2W Technologies, Inc., CA) (Figure 3.1c) was developed. Voice coil motors have several advantages over other linear actuation schemes including its small size, high force to weight ratio, and high accelerations. Figure 3.1d shows the schematic diagram of the voice coil motor experimental setup. A function generator (33220A, Agilent Technologies, Inc., CA) was utilized to provide the actuation signal for controlling the voice coil motor motion. This was followed by a current amplifier for amplifying the signal to drive the motor due to its low electronic impedance (~1Ω). The current amplifier was constructed based on a non-inverting unity gain buffer circuit using a power operational amplifier (Op-Amp) (LM675, National Semiconductor Corp., CA) as shown in Figure 3.1e, and a DC power supply (1670A, B&K Precision Corp., CA) was employed to provide the DC voltage for the Op-Amp operation. The output signal from the amplifier was then connected to the motor. The voice coil motor was housed in a custom made acrylic stage on which the PDMS microdevices can be easily attached (Figure 3.1b). In addition, a brass bolt with a semispherical head was connected to the

motor, forming the contact surface with the PDMS membrane when stretching. The brass bolt head moved upwards to deform the PDMS membrane (Figure 3.2).

ANSYS Finite Element Analysis (FEA)

In order to estimate the strain generated on an elastomeric PDMS membrane top surface while the membrane is deformed by the linear actuation motion, we performed simulations using finite element analysis (FEA) software, ANSYS 10.0 (ANSYS Inc., Southpointe, PA). To reduce the computational time, a 2-D model with an axis symmetric boundary condition was constructed. The model was composed of a flat membrane and a curved head structure, where the bolt head structure was assumed to be rigid (Figure 3.3a). Contact analysis was performed to simulate the interaction between the two objects. Contact and target elements, CONTA172 and TARGE169, were assigned on the bolt head and the membrane bottom surface to simulate the surface-to-surface contact. The membrane was simulated using triangular 2-D elements, PLANE2. The axis symmetric boundary condition was assigned along the Y-axis, and one end of the membrane was assigned the fixed boundary condition. The displacement boundary condition, which was measured experimentally, was assigned to the bolt head. To simulate the large deformation of the PDMS membrane, non-linear, large deformation static analysis was performed. For all simulations, a Young's Modulus of 750 kPa and a Poisson's Ratio of 0.49 for the PDMS membrane were used.

Cell experiments

Stretching with air-liquid interface versus no interface

Five 6-mm diameter wells seeded with A549 epithelial cells were used in experiments to determine the effect of cyclic stretching with and without an air-liquid

interface. One well was used as the control where cells were neither exposed to an air-liquid interface nor stretched. Two of the remaining wells were maintained under "normal" conditions which referred to cells covered with a large supply of media (50 μl) within the well. The liquid in the remaining 2 wells was aspirated and replaced with a small volume (6 μl) of media creating a thin film of liquid over the bottom surface of the well. The 4 wells were then exposed to stretching protocols with the linear actuator programmed to move the pin head up and down cyclically at a frequency of 1 Hz. The cells in 2 sets of wells (one under normal conditions and one with 6 μl media) were exposed to stretch for 30 seconds, and 2 sets were exposed to 90 seconds of stretch. After mechanically stretching the wells, each well was filled with growth media and placed in an incubator for 10 minutes prior to staining.

Effect of liquid volume on stretching

To determine the effect of the volume of liquid in the wells during stretching, 4 wells cultured with A549 cells were filled with 3, 10, 20, and 30 μl of culture media respectively. The wells were then exposed to cyclic stretch at 0.2 Hz frequency for 30 seconds, and filled with media for 10 minutes prior to staining.

Effect of the number of stretches for cell death

To estimate the number of stretches required to damage the cells, wells were stretched at a frequency of 0.2 Hz for one, five, six, seven, eight and ten stretches. After the specified number of stretches, the wells were incubated with media for 10 minutes before staining.

Effect of surfactant

To test the effect of surfactant on protecting the cells from injury, instead of 6 µl of media, 6 µl of Survanta (beractant), a sterile pulmonary surfactant, diluted to 1 mg/ml in serum-free culture media was used to coat the cells while stretching at 0.2 Hz for 30 seconds.

Fluorescence cell staining

Cell were stained using the LIVE/DEAD Viability/Cytotoxicity kit for mammalian cells (Invitrogen). Upon entering live cells, Calcein AM is converted into its green fluorescent form (ex/em 495 nm/515 nm) and is retained within the cell. Ethidium homodimer-1 (EthD-1) enters cells with damaged membranes and fluoresces red (ex/em 495 nm/635 nm) upon binding to the nucleic acids. EthD-1 is excluded by intact live cells and is therefore a marker of dead cells.

To stain the cells, 5 µl of a 4mM Calcein AM solution diluted in DMSO (ATCC) and 5 µl of 2mM EthD-1 in DMSO/H_20 1:4 (v/v) were diluted into 490 µl of growth media. 50 µl of this solution was then pipetted into each of the wells and allowed to incubate in the dark for 15 minutes.

All images were taken using Simple PCI imaging software program (Compix Inc. Cranberry Township, PA) connected to a CCD camera (Hamamatsu Orca-ER) mounted on an inverted phase contrast/fluorescence microscope (TE-300, Nikon, Tokyo) using the 4x and 2x objectives.

3.3 Results

FEA Analysis

Figure 3.3b shows the results obtained from the FEA simulation of the estimated levels of tangential and radial strains associated with the top surface of the PDMS membrane.

Cell experiments

Figure 3.4b,c shows the results obtained from stretching A549 cells under normal conditions and using an air-liquid interface for 30 and 90 seconds at 1 Hz. Live cells are stained green while the nuclei of dead cells are stained red. A control well with cells exposed to neither an air-liquid interface nor stretching is shown in Figure 3.4a. Figure 3.5 shows the results obtained from stretching cells in wells containing volumes of liquid ranging from 3 to 30 μl of media. Figure 3.6a-f shows the results of stretching cells using an air-liquid interface at 0.2 Hz with varying number of stretches ranging from one stretch (Figure 3.6a) to 10 stretches (Figure 3.6f). The results of cells stretched using 6 μl of media versus 6 μl of Survanta are shown is shown in Figure 3.1.

3.4 Discussion

ARDS lungs and atelectasis

Lungs injured with ARDS are generally divided into three regions: (1) regions where alveoli are collapsed at end expiration due to interstitial infiltration and open during inspiration, (2) regions where the air spaces are filled with exudates (alveolar edema) and not available for gas exchange, and (3) aerated normal lung, which can often be reduced to as low as 25% of normal lung volume in diseased lungs (Slutsky 1998). A common pathologic finding in ARDS is diffuse alveolar damage characterized by neutrophil accumulation and damage to the epithelium resulting in increased permeability, transudation of protein-rich fluid into the interstitial and alveolar spaces and

loss of pulmonary epithelial cells. Mechanical ventilation with high volumes can further the damage and lead to the development of VILI.

The ability of increased ventilation volumes to damage epithelial cells has been well documented in both humans and animals (Levine 2006). However, what remains unknown is the source of the damaging aspects of MV that can lead to VILI. One theory is that the repetitive opening and closing of alveoli and the associated high shear stresses is the most damaging to the integrity of the alveolar epithelium. In a nonuniformly expanded lung, a transpulmonary pressure of 30 cm H_2O is equivalent to a pressure of 140 cm H_2O in the atelectatic regions (Ricard 2001), which can lead to considerable cell disruption and rupture. Efforts to study the effects of VILI have focused on the alveolar epithelium: an integral part of the blood-air barrier that facilitates the efficient clearance of alveolar edema in response to injury (Crandall 1991).

Stretching systems

There is a growing interest in studying the mechanisms that link mechanical forces such as cyclic stretch and shear with injury. To do so, one of the most common methods is using cell stretching devices where cells are cultured on deformable substrates. Several biaxial cell strain devices have been used to apply strain on lung cells (Buck 1980, Dartsch 1986) by repeated mechanical deformations of a membrane on which cells are attached. One type of device consists of the deformation of a thin, elastic cell culture substrate using positive or negative pressure, such as in the commercially available Flexcell system (Banes 1985, Wirtz 1990) or through a uniaxial cyclical stretch (Kato 1998). Other devices include ones in which strain is applied using a magnetic

force (Mourgeon 1999) or from the elongation of foam sponges that are seeded with cells (Liu 1992).

Alveolar epithelial cells and cyclic stretch

Mechanical stimuli have been shown to have many effects on alveolar type II cells including stimulating calcium signaling, phospholipids secretion, and surfactant protein expression. Adverse effects such as apoptosis, cell membrane stress failure, and cell death have also been known to occur (Hammerschmidt 2004). It has been shown that the basement membrane of the epithelial cells undergoes expansion as lung volumes approach physiologic limits and experiences significantly larger deformations during MV (Tschumperlin 2000).

Previous studies have examined the effects of stretching on alveolar epithelial cells. Tschumperlin et al. exposed primary type II alveolar cells (ATII) to mechanical stretch and found that injury to the cells, measured with a LIVE/DEAD stain increases with strain magnitude and duration and decreases with cellular seeding density and time elapsed after seeding (Tschumperlin 1998). In another study, they also determined that deformation-induced injury depends on repetitive stretching, with cyclic deformations more damaging than static stretch. Cell death occurred within the first hour, with more than two-thirds of the cells dead within 5 minutes (Tschumperlin 2000). These studies showed that injury to the lungs is modest when deformations are less than that under total lung capacity (TLC), but the extension of the findings to the alveolar environment with air-liquid interfaces has not been studied.

Fluid mechanical stresses

In vivo, mechanical forces can arise from a variety of sources such as dynamic compression, interstitial fluid flow, or tension. Fluid motion generates dynamic shear forces at surfaces and simultaneously increases mass transfer and hydrodynamically stimulates cells at the tissue-fluid interface through fluctuations in the fluid velocity and stresses. Shear stress, or the tangential component of hemodynamic forces acting on the wall, is an important modulator of cell functions in both normal and pathological conditions (Ku 1985). Excessive shear has been found to induce cell deformation, cause plasma membrane disruption and gross tearing, and ultrastructural injury to the alveolar wall (Carney 2006).

In injured lungs, the cells of the alveolar epithelium are also exposed to fluid mechanical strains originating from the propagation of liquid plugs to reopen collapsed airways and alveoli. During reopening, a finger of air progresses down a collapsed airway, generating large and rapid changes in normal and shear stresses along the walls. A commonly used system to study this type of injury is the rigid parallel-plate chamber in which a semi-infinite bubble is propagated down a fluid-occluded channel lined with pulmonary epithelial cells. Using such a system, Bilek et al. showed that the steep pressure gradient near the bubble front was major determinant of the degree of lung injury in surfactant-deficient situations. The addition of surfactant alleviated this injury (Bilek 2003). Other systems include the microfluidic airway system developed by Huh et al. in which the propagation and rupture of liquid plugs across airway epithelial cells lead to significant cell injury (Huh 2007).

Stretching with an air-liquid interface

Although these studies have provided valuable information about cellular behavior under mechanical strain, none have considered the effects of cyclic strain on cells stretched with an air-liquid interface where cells are exposed to both deformations resulting from the solid substrate (cyclic radial strain) and also from the fluid (fluid mechanical stresses). What is needed is an *in vitro* model of VILI where alveolar epithelial cells are exposed to both substrate stretching and fluid mechanical stresses. Our studies have focused on the effects of cyclic stretch combined with the movement of an air-liquid interface on alveolar epithelial cells. It is believed that cellular injury associated with inflating the lungs and deforming the alveolar epithelium plays a major role in the development of VILI. We test the idea that it is both stresses originating from the substrate and the fluid mechanical stresses that is the major cause of injury arising from MV. Even modest tidal volumes such as that encountered during normal ventilation can be damaging to injured lungs filled with a protein-rich alveolar edema. The addition of surfactant can serve to protect the epithelium from this type of injury.

The linear actuator system described here is able to recreate this air-liquid interface. By using small volumes of liquid and extending the bolt head a certain distance, cells in the middle of the well are exposed to the movement of a very thin layer of fluid when stretched (Figure 3.1c).

By exposing type II alveolar epithelial cells to radial stretch with an air-liquid interface using the device shown in Figure 3.1a, we have found that considerable cell death can occur within 30 seconds of stretch at 1 Hz (Figure 3.3b). Cells that do not encounter an air-liquid interface do not show significant amounts of injury even after 90

seconds of stretch (Figure 3.3c). To determine if it is the location of the meniscus of the air-liquid interface that is most damaging to the cells, the cells were stretched with wells containing various amounts of media, thereby changing the location of the meniscus. When containing small amounts of liquid (3 μl), the meniscus is expanded to near the edges of the well, and as shown in Figure 3.4a, the damage to the epithelial cells occurs within this wide range. As the amount of liquid increases, the number of cells exposed to the thin film of liquid decreases, and the amount of damage is restricted to smaller areas (Figure 3.4 b,c) until there is no air-liquid interface (Figure 3.4d). To estimate the number of stretches required for cell damage, cells were stretched with a varying number of stretches. From Figure 3.5, it can be seen that cells stretched up to 5 times show little damage, however between 6 and 10 stretches, the cells begin to die. The addition of Survanta, a commercially available surfactant abrogates the damage caused by the movement of the air-liquid interface (Figure 3.1d).

Degree of strain

Due to the complexity of the local distension patterns within the lung parenchyma during ventilation, it is difficult to quantify the degree of strain *in vivo* as well as to translate lung volume changes to changes in cell strain. Several *in vitro* models have determined that changes in epithelial basement membrane surface area (EBMSA) of 12-30% reflect lung inflations from 75-100% of total lung capacity (TLC) (Tschumperlin 1998). Percent changes in EBMSA can also be higher during MV with high tidal volumes and exceeded in parts of the lung remaining open following derecruitment. Using the present system, the cells are exposed to nonuniform strains with maximal radial strains between 10-12% (Figure 3.3). The nonuniformity of strains is similar to *in vivo*

cell deformations which are most likely to be heterogeneous. Within the alveolar perimeter, there can also be marked differences in the amount of distension. When distending an alveolar perimeter to 14%, it has been found that different segments within the same alveolus can distend anywhere from 5-25% (Perlman 2007).

In humans, it has been found that changes in surface area (SA) of 25% (corresponding to inflations up to 80-85% of TLC) can occur during vigorous exercise in humans without loss of pulmonary epithelial barrier function (Cavanaugh 2002) while an amplitude that has been found to be characteristic of MV is between a 20-30% change in SA (Trepat 2006). A 50% change in SA is thought to be representative of regional overinflation in diseased lungs (Tschumperlin 1998). The problem arises in ARDS lungs when mechanical strains are inflicted upon already diseased lungs with preexisting lung injury that are filled with edema. The filling of the small airways, alveoli, and interstitial spaces with cells and fluid alters the normal relationship between strain and plasma membrane recovery during MV. The deleterious effects of MV may be amplified in diseased lungs. In the system described here, percent changes in surface area average approximately 7% throughout the entire membrane surface which is closer to that encountered during normal ventilation. Larger percent changes in surface area can potentially be achieved by extending the pin head upwards a greater distance, decreasing the thickness of the PDMS membrane, or increasing the size of the well.

Models of the alveolar epithelium

It is noted that this cell culture system with A549 cells is an oversimplification of the lung structure and the complex forces involved in mechanical ventilation. The alveolar epithelium is not readily accessible for study due to the complex architecture of

the lung; therefore researchers have turned to using lung cell cultures as an *in vitro* model of the alveoli. To study properties of the alveolar epithelium, the human A549 Type II alveolar epithelial cell line is often used. The A549 cell line, derived from an alveolar cell carcinoma of the lung, is a good substitute in that the cells retain its cuboidal shape in culture, contain lamellar bodies and microvilli, synthesize lectin and phosphatidylcholine (components of surfactant), and can release and/or express cytokines and growth factors (Robinson 1984). However these cells often lack the full differentiated phenotype of the *in vivo* cell and remain controversial as a cultured model of alveolar epithelial cells. For example, A549 cell cultures are unable to create a restrictive barrier, instead forming a monolayer with high permeability and less tight junctional proteins. A recent study, however, has shown that when grown to confluence, A549 cell cultures can form adherens junctions and tight junctions (Trepat 2006).

Primary cultures of ATII cells (most commonly from a rat) are able to generate monolayers that resemble the pulmonary epithelium when cultured on semi-permeable polycarbonate membranes for 5 to 8 days. However most cultures have proven difficult to establish, with low viability and are difficult to purify due to contamination with other cells. It has also been shown that Type II cells in culture eventually transdifferentiate into Type I cells, acquiring biochemical and morphological changes such as the loss of microvilli, increase in cell surface area, and development of thin cytoplasmic attenuations characteristic of ATI cells (Brody 1989). Due to the difficulty in obtaining and maintaining these primary cell cultures, A549 cells have been used here as a simple model that captures the essential features of the alveolar epithelium.

Surfactants are wetting agents that coat the inner surface of alveoli. They help to inflate and expand the alveoli by reducing the surface tension at the air-liquid interface and preventing alveolar collapse at exhalation. Surfactant is naturally produced in healthy lungs, however ARDS patients suffer from a deficiency or dysfunction of surfactant, causing stiff lungs that make breathing difficult. This also occurs in premature babies with under-developed lungs that are incapable of producing surfactant. Exogenous surfactant preparations have been used for both the treatment and prevention of respiratory distress syndrome. Survanta (Beractant, Abbott Laboratories, North Chicago, IL) is a sterile, non-pyrogenic commercially available surfactant that is commonly given to premature babies through endotracheal administration. Survanta is a natural bovine lung extract supplemented with dipalmitylphosphatidylcholine, tripalmitin, and palmitic acid (Soll 1990) to mimic the surface-tension lowering properties of natural lung surfactant. When administered to the lungs of premature infants, Survanta replenishes surfactant and restores the surface activity in the lungs. In experiments done by Bilek et al., the addition of surfactant reduced the amount of epithelial cell injury caused by the propagation of an air bubble down an artificial airway (Bilek 2002). The addition of 1 mg/ml of Survanta to our system reduced the amount of damage done to alveolar epithelial cells when stretched for 30 seconds using an air-liquid interface when compared to cells stretched using culture media (Figure 3.1d).

3.5 Conclusions

The development of therapies that prevent or modulate the harmful effects of VILI is dependent upon the understanding of the cellular mechanisms underlying this type of lung injury. We have shown that cells stretched using an air-liquid interface

results in greater damage than without the interface. Such air-liquid interfaces are more characteristic of physiological conditions such as that found in injured fluid-filled alveoli. The addition of surfactant abrogates the amount of cell injury. The system described here allows us to incorporate both solid substrate deformations and fluid mechanical stresses. This study was able to address the behavior of cells in a mechanically active environment and further our understanding of the biomolecular and cellular effects of exposing the lung to a combination forces commonly encountered in patients with mechanical ventilation. The device is useful in that complicating variables such as changes in blood gases and inflammatory responses found in *in vivo* studies are eliminated. The results can have further implications in ventilator management and surfactant therapy for patients suffering from ARDS or ALI.

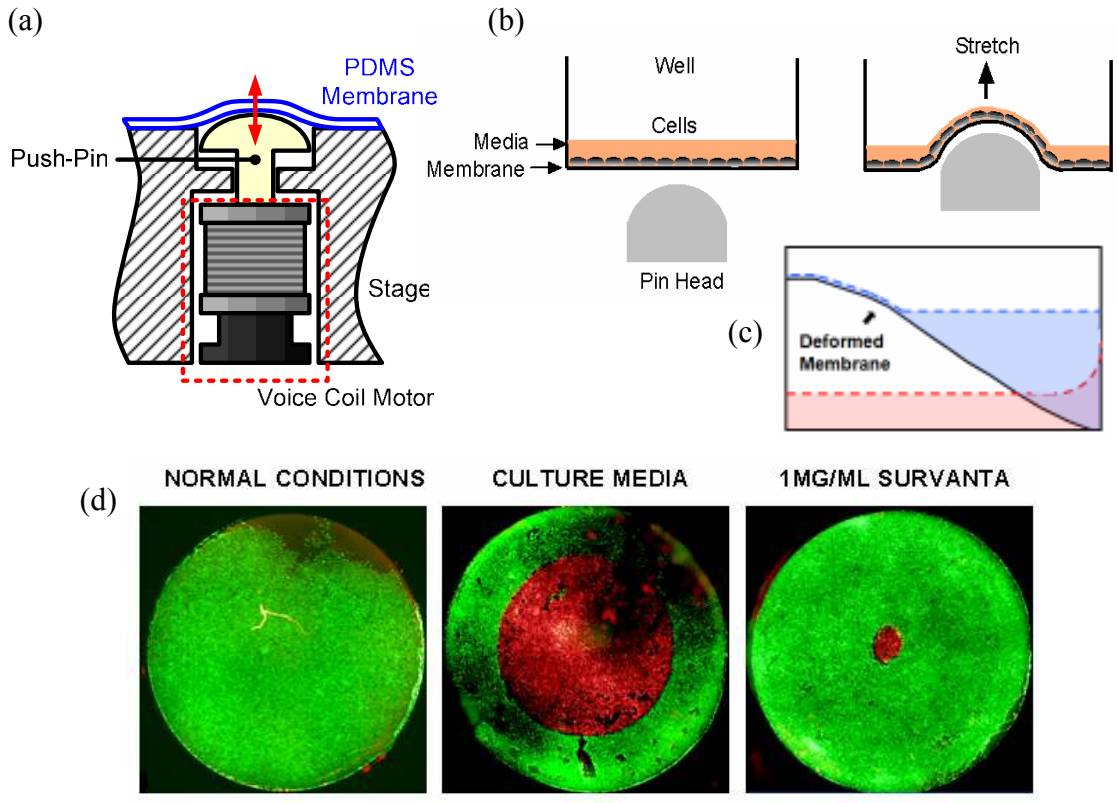

Figure 3.1: Stretching alveolar epithelial cells using an air-liquid interface. (a) Schematic view of voice coil motor and attached push-pin head deforming PDMS membrane. (b) Schematic of the side view of a well with cells cultured on the deformable bottom membrane. A thin layer of media covers the cells (left). When the membrane is stretched by the pin, the cells are exposed to an air-liquid interface (right). A close up of this interface is shown in (c). (d) Fluorescent images of A549 alveolar epithelial cells stained with a LIVE/DEAD stain. Cells were stretched in media with no interface (left), with 6 µl media for 30 seconds at 0.2 Hz with air-liquid interface (middle) or with 6 µl of 1mg/ml Survanta for 30 seconds at 0.2 Hz (right). Surfactant reduces damage even with air-liquid interface.

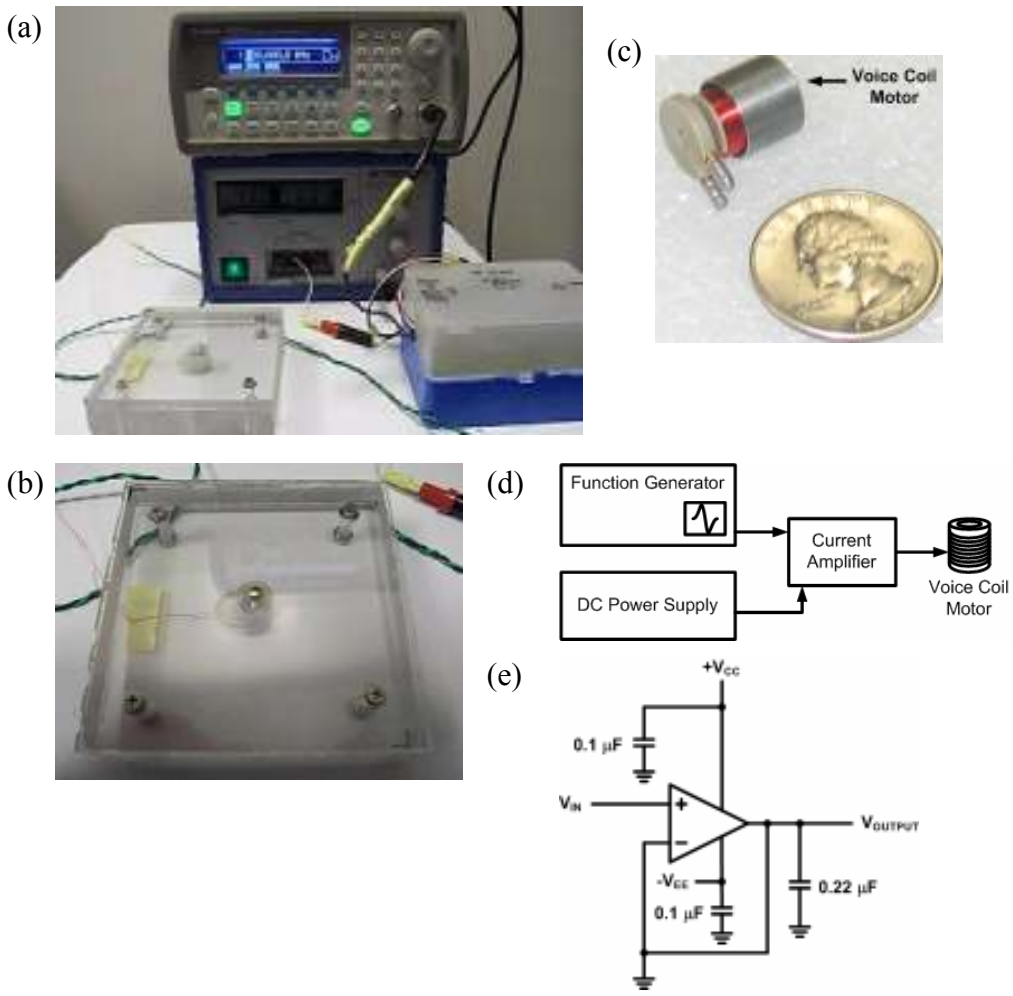

Figure 3.2: (a) Setup for the linear actuator. (b) The voice coil motor (c) housed in an acrylic stage. (d) Schematic diagram for voice coil motor experimental setup. (e) A non-inverting unity gain buffer circuit based on Op-Amp for current amplification.

.

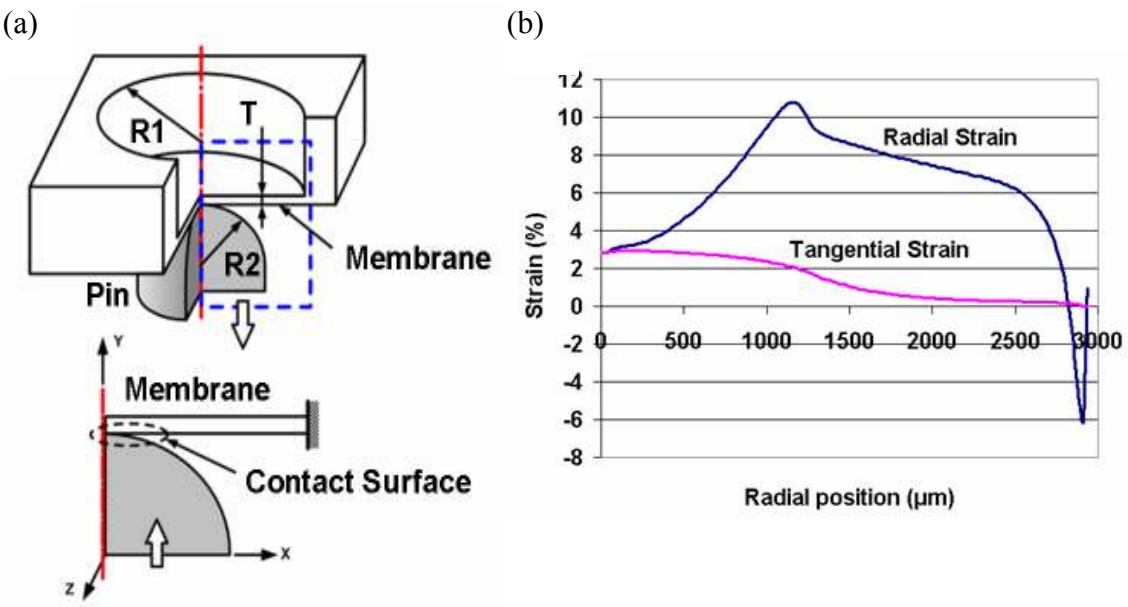

Figure 3.3: ANSYS Finite Element Analysis simulation of membrane stretching. (a) 2-D model for pin (radius R2) contacting a microwell (radius R1) with a flexible bottom membrane (thickness T). (b) Simulated radial and tangential strains on membrane surface.

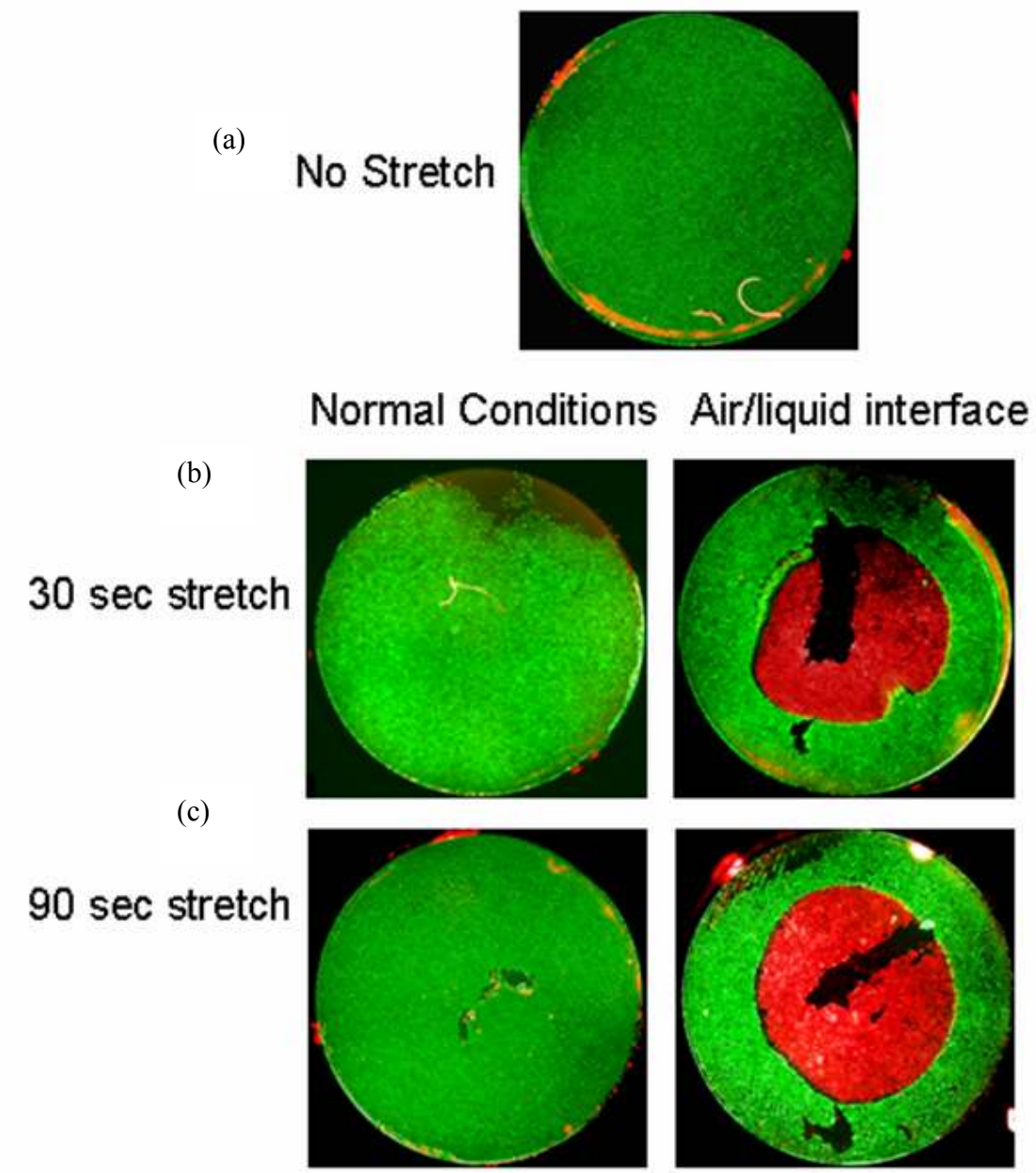

Figure 3.4: Fluorescent images of A549 alveolar epithelial cells stained with a LIVE/DEAD stain. Top: Control well of cells grown under normal conditions. Cells stretched for 30 seconds (b) and 90 seconds (c) at 1 Hz under normal conditions (left) and with an air-liquid interface (right). Wells are 6 mm in diameter. Live cells are stained green, while the nuclei of dead cells are stained red.

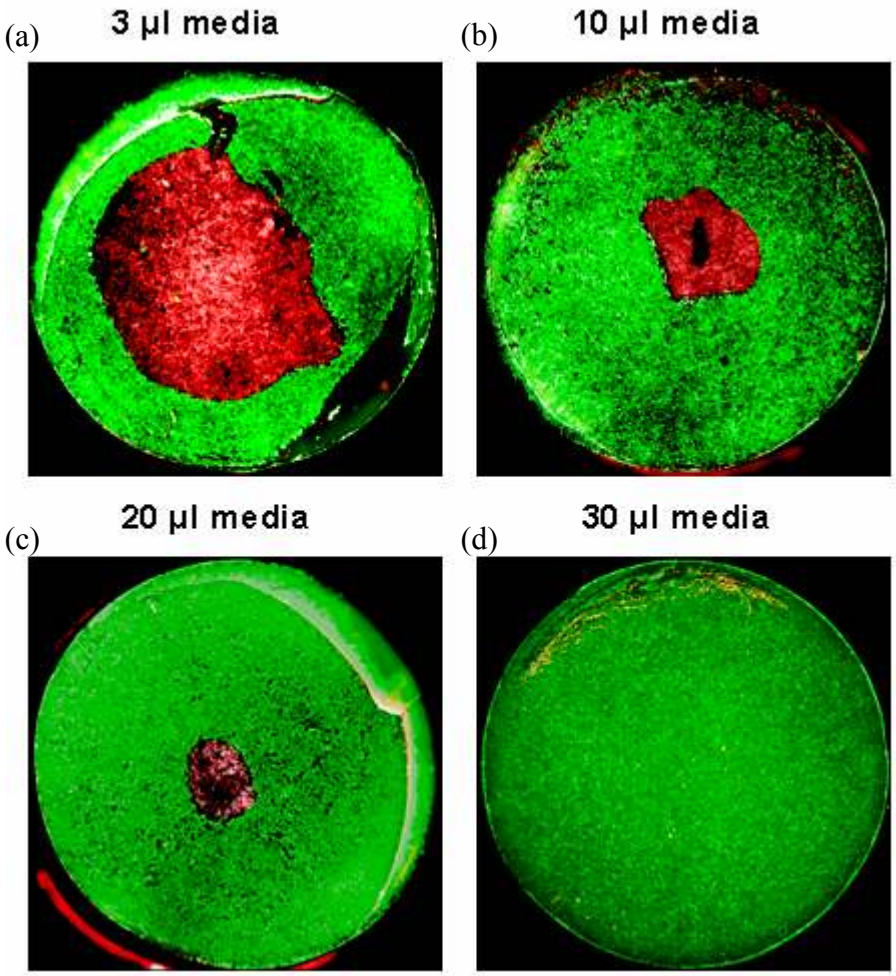

Figure 3.5: Fluorescent images of A549 alveolar epithelial cells stained with a LIVE/DEAD stain. Cells stretched for 30 seconds at 0.2 Hz with wells containing (a) 3 µl, (b) 10 µl, (c) 20 µl, and (d) 30 µl of media. Wells are 6 mm in diameter. Live cells are stained green, while the nuclei of dead cells are stained red.

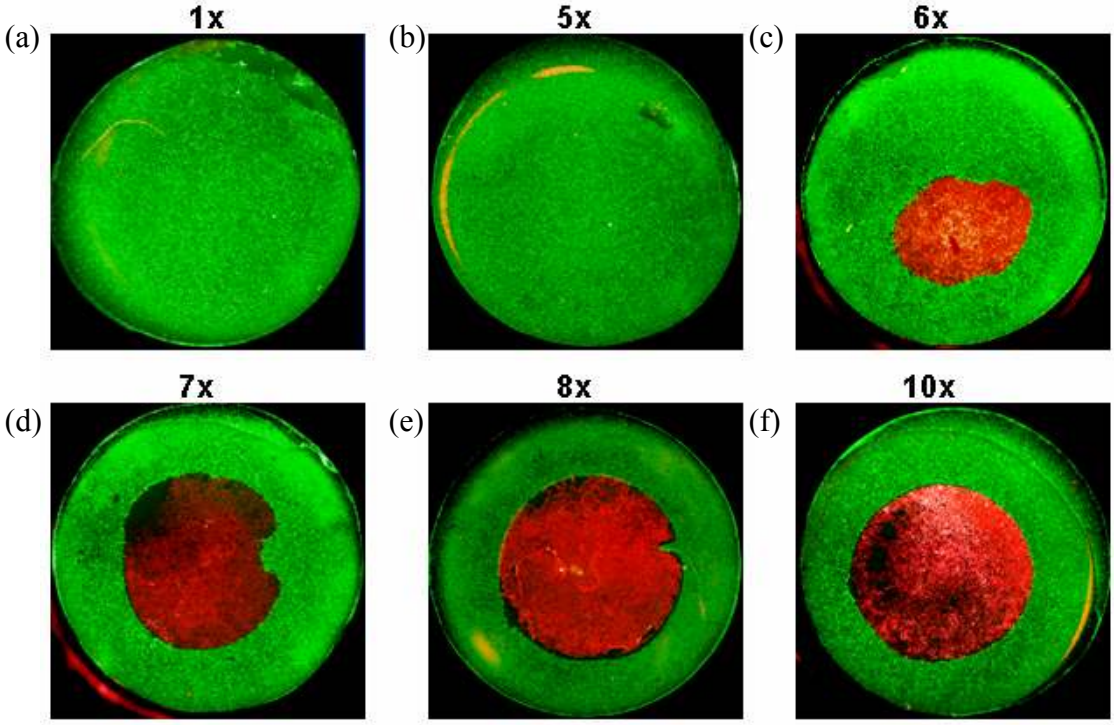

Figure 3.6: Number of stretches until cell damage. Cells were stretched using an air-liquid interface at 0.2 Hz for (a) one, (b) five, (c) six, (d) seven, (e) eight, and (f) 10 stretches.

3.6 References

Banes AJ, Gilbert J, Taylor D, Monbureau O. A new vacuum-operated stress-providing instrument that applies static or variable duration cyclic tension or compression to cell in vitro. J. Cell. Sci 1985;75: 35-42.

Bezzant TB, Mortensen JD. Risks and hazards of mechanical ventilation: a collective review of published literature. Disease-a-Month. 1994;40: 581-640.

Bilek AM, Dee KC, Gaver III DP. Mechanisms of surface-tension-induced epithelial cell damage in a model of pulmonary airway reopening. J. Appl. Physiol. 2003;94:770-783.

Brody JS, Williams MC. Pulmonary alveolar epithelial cell differentiation. Annu. Rev. Physiol. 54; 351-371. 1992.

Buck RC. Behavior of vascular smooth muscle cells during repeated stretching of the substratum in vitro. Atherosclerosis 1983;46:217-223.

Carney D, DiRocco J, Nieman G. Dynamic alveolar mechanics and ventilator-induced lung injury. Crit Care Med. 2006; 33: S122-S128.

Cavanaugh KJ, Margulies SS. Measurement of stretch-induced loss of alveolar epithelial barrier integrity with a novel in vitro method. Am J Physiol Cell Physiol. 283: 1801-1808. 2002.

Crandall ED, Kim KJ. Alveolar epithelial barrier properties. In: The Lung: Scientific Foundations, edited by RG Crystal and JB West. New York: Raven, 1991, 273-287.

Dartsch PC, Betz E. Response of cultured endothelial cells to mechanical stimulation. Basic Res Cardiol. 1989; 84:268-281.

Frangos JA, L. V. McIntire and S. G. Eskin, Shear-stress induced stimulation of mammalian-cell metabolism, Biotechnol. Bioeng., 32: 1053-1060, 1988.

Hammerschmidt S, Kuhn H, Grasenack T, Gessner C, Wirtz H. Apoptosis and necrosis induced by cyclic mechanical stretching in alveolar type II cells. Am J Respir Cell Mol Biol. 30; 396-402. 2004.

Huh D, Fujioka H, Tung Y-C, Futai N, Paine III R, Grotberg JB, Takayama S. Acoustically detectable cellular-level lung injury induced by fluid mechanical stresses in microfluidic airway systems. PNAS. 2007;104:18886-18891.

Kato T, Ishiguro N, Iwata H, Kojima T, Ito T and K. Naruse, Up-regulation of cox2 expression by uni-axial cyclic stretch in human lung fibroblast cells., *Biochemical and Biophysical Research Communications*, 244: 615-619, 1998.

Ku DN, Giddens DP, Zarins CK, Glagov S. Pulsatile flow and atherosclerosis in the human carotid bifurcation. Positive correleation between plaque location and low oscillating shear stress. *Arteriosclerosis* 5; 293-302, 1985.

Levine GK, Deutschman CS, Helfaer MA, Margulies SS. Sepsis-induced lung injury in rats increases alveolar epithelial vulnerability to stretch. Crit care Med. 34; 1746-1751. 2006.

Liu M, Skinner SJM, Xu J, Han RNN, Tanswell AK, Post M. Stimulation of fetal rat lung cell proliferation in vitro by mechanical stretch. *Am J Physiol.* 263; L376-L383. 1992.

Mourgeon E, J. Xu, K. Tanswell, M. Liu and M. Post, Mechanical strain-induced posttranscriptional regulation of fibronectin production in fetal lung cells, American Journal of Physiology, 277: L142-L149, 1999.

Olesen SP, Clapham DE, Davies PF, Hemodynamic shear stress activates a k+ current in vascular endothelial cells, *Nature*, 331: 168-170, 1988.

Paine III R, Simon RH. Expanding the frontiers of lung biology through the creative use of alveolar epithelial cells in culture. Am J. of Physiol. 270 (4): L484-L486 APR 1996.

Perlman CE, Battacharya J. Alveolar expansion imaged by optical sectioning microscopy. J Appl Physiol 2007;103:1037-1044.

Ricard JD, Dreyfuss D. Cytokines during ventilator-induced lung injury: A word of caution. *Anesth Analg.* 93: 251-2. 2001.

Robinson PC, Voelker DR, Mason RJ. Isolation and culture of human alveolar type II epithelial cells. Am.Rec.Repir.Dis. 130: 1156-1160, 1984.

Schumacker PT. Straining to understand mechanotransduction in the lung. Am J Physiol Lung Cell Mol Physiol 2002;282: L881-L882.

Slutsky AS, Tremblay LN. Multiple system organ failure; is mechanical ventilation a contributing factor? Am J Respir Crit Care Med. 1998;157: 1721-1725.

Soll RF, Hoekstra RE, Fangman JJ, Corbet AJ, Adams JM, Stanley JL, Schulze K, Oh W, Roberts JD, Dorst JP, Kramer SS, Gold JA, Zola EM, Horbar JD, McAuliffe TL, Lucey JF. Multicenter trial of single-dose modified bovine surfactant extract (Survanta) for prevention of respiratory distress syndrome. Pediatrics 1990;85:1092-1102.

Trepat X, Puig F, Gavara N, Fredberg JJ, Farre R, Navajas D. Effects of stretch on structural integrity and micromechanics of human alveolar epithelial cell monolayers exposed to thrombin. Am J Physiol Lung Cell Mol Physiol 290; 1104-1110. 2006.

Tschumperlin DJ, Margulies SS. Equibiaxial deformation-induced injury of alveolar epithelial cells in vitro. Am J Physiol. 1998; 19: L1173-L1183.

Tschumperlin DJ, Oswari J, Margulies SS. Deformation-induced injury of alveolar epithelial cells. Am J Respir Crit Care Med. 2000; 162: 357-362.

Whitesides GM, Ostuni E, Takayama S, Jiang XY, Ingber DE. Soft lithography in biology and biochemistry. Annu. Rev. Biomed. Eng., 2001; 3: 335-373.

Wirtz HR., Dobbs LG. Calcium mobilization and exocytosis after one mechanical stretch of lung epithelial cells. Science 1990; 250: 1266-1269.

Chapter 4

Microfluidic Immunoassay using a Braille Display for Computer-controlled Fluid Actuation

Microfluidic immunoassays overcome the limitations of conventional assay systems with its enhanced reaction efficiency, simplified procedures, and reduced consumption of reagents. Available microfluidic systems, however, have large external fluid controls and multiple fluidic interconnects. We have developed a self-contained, connectorless, automated microfluidic immunoassay system to detect and quantify levels of Interleukin (IL)-8, an important cytokine involved in the inflammatory response. In our microfluidic system, liquid flow is controlled using the pins of a commercially available, refreshable Braille display that act as small mechanical actuators. A bead-based sandwich assay was used to detect the release of IL-8 from alveolar epithelial cells cultured on-chip and stimulated with tumor necrosis factor-α. Integration of the microfluidic immunoassay system with cell culture provides a novel, self-contained device to analyze the by-products of chemically stimulated cells in a controlled microenvironment.

4.1 Introduction

In fields such as cellular biology and biochemical detection, it is important to be able to accurately detect and quantify the concentration of small amounts of biological proteins in solution. One of the most common methods to do so is the immunoassay

which is a relatively fast, sensitive, and reliable analytical method for detecting biological molecules used in clinical diagnosis, environmental analyses, and biochemical studies. Immunoassays take advantage of the high specificities of antibodies to the molecule of interest making them ideal for analyzing small amounts of proteins with high sensitivity. Conventional sandwich immunoassays involve 96-well microtiter plates where the antigen-specific capture antibody is noncovalently adsorbed onto the well surface. Subsequent detection is done using a secondary antibody coupled to either an enzyme, or a fluorophore. The signal intensity level is proportional to the amount of bound analyte. Disadvantages to these systems include: long assay times (often several hours), the use of large quantities of expensive reagents, and numerous washing and incubation steps. Even though the antibody-antigen reaction is a rapid process, long incubation times are required due to the inefficient mass transport of molecules that diffuse from the solution onto the surface where the reaction occurs.

There is a growing trend towards creating systems that can be miniaturized and integrated such as 'lab-on-a-chip' devices and micro-total analysis systems (μ-TAS). An alternative to conventional analytical systems, these microfabricated devices integrate several steps such as sampling, sample preparation, reaction, and detection on a single chip. These systems take advantage of microfluidics, a field where fluid control is achieved through microscale pumps, valves, sensors, and actuators. Microfluidics is a promising area for miniaturizing assays as immunoassays performed in microchannels are able to overcome the limitations of conventional systems with its enhanced reaction efficiency, simplified procedures, and greatly reduced consumption of reagents and samples. There is the potential for automated fluid delivery with precise manipulation of

small volumes of fluid, analysis of multiple samples close to the length scale of interest (eg. cells, proteins), and point-of-care testing. Microfluidic channel systems can be developed in various forms involving differences in the channel structure (Lai 2004, Hatch 2001), solid substrate (Eteshola 2001, 2004, Jiang 2003), separation (Yeung 2003), sample transport (Linder 2002), and detection (Abdel-Hamid 1998, Schweitzer 2000,2002). An additional advantage is the ability to perform integrated analysis of nanoliter volumes of media conditioned by cells cultured in microfluidic systems. However, the disadvantage is that the individual elements of the microsystem as well as the microchip are often complicated to fabricate and integrate. Quake et al. have created a pneumatic valve/pump system for microchannels, however it involves multiple components and external connections (Unger 2000).

To overcome some of these limitations, we have developed a self-contained, connection-less, automated microfluidic immunoassay system. This system is fabricated with Poly(dimethylsiloxane) (PDMS) and liquid flow is controlled using small mechanical actuators provided by the pins of a commercially available, refreshable Braille display. The system uses the elastomeric properties of PDMS to valve off channels by deforming the thin, bottom layer of microchannels. A combination of three pins in a specific sequence allows for the uni-directional pumping of fluid (Gu 2004). The Braille system allows us to incorporate multiple, miniaturized pumps and valves that function independent of each other and is portable, versatile, and cost-effective. The display is also controlled using a program configured to manipulate the sequence of pins for fluid actuation. Microbeads coated with the primary antibody are packed into the channel and held in place through small magnets embedded above the channel regions

designated for the immunoassay. The antigen of interest is flowed through the system, and its presence is detected using a fluorescently labeled secondary antibody.

Cells secrete many chemicals into their surroundings including signaling molecules, trophic factors, and metabolic products. Measurements of these chemicals are often performed off-chip after collecting a sample of the cell perfusate. Microfluidic systems offer the potential to develop chips where both cell culture is maintained and measurements are performed downstream. Examples of previous systems include the microfluidic device developed by Kennedy et al. to monitor the secretion of insulin from islet cells with continuous sampling and a rapid electrophoresis-based immunoassay (Shackman 2005). Other examples include systems to measure nitric oxide release from macrophage-like cells (Goto 2005) and an on-chip microculture system for differential analysis of single cells (Inoue 2001). Such systems however require special assay development different from commercial systems. We have developed a simple microfluidic system capable of on-chip analysis of the biochemical responses of cells to cytokine exposure.

Here, we describe how the microsystem can be used to detect and quantify Interleukin (IL)-8, an important cytokine involved in neutrophil recruitment and activation during the inflammatory response. The ability to do so will prove beneficial for biological studies of cell responses to the micro-physiological conditions recreated on microfluidic chips. To demonstrate the application of the system to analyze biological samples, an assay to detect IL-8 released from alveolar epithelial cells cultured on-chip was performed.

4.2 Materials and Methods

Reagents

N-Hydroxysulfosuccinimide sodium salt, N-(3-Dimethylaminopropyl)-N'-ethylcarbodiimide, and sodium azide were purchased from Sigma Aldrich (St. Louis, MO) and diluted in PolyLink Coupling Buffer (50 mM MES, pH 5.2, 0.05% Proclin 300) from Bangs Labs Inc (Fishers, IN) before use. COMPEL Magnetic COOH modified microspheres (8.27 μm diameter) were also purchased from Bangs Labs Inc. Purified mouse anti-human IL-8 monoclonal antibody (unconjugated, ELISA capture) and biotinylated mouse anti-human IL-8 monoclonal antibody (ELISA detection) were purchased from BD Biosciences (San Jose, CA). Recombinant human Interleukin-8 (IL-8) was purchased from eBioscience (San Diego, CA) and streptavidin conjugated to AlexaFluor 594 from Molecular Probes (Invitrogen, Carlsbad, California). StartingBlock T20 (PBS) Blocking Buffer (includes 0.05% Tween-20 Detergent) was purchased from Pierce Chemicals (Rockford, IL) and used as received. The A549 cell line was obtained from ATCC (Manassas, VA) and the recombinant human TNF-α from Cell Sciences (Canton, MA). All solutions except the beads were centrifuged before use to remove unwanted particles.

Device fabrication

The microchannels of the immunoassay microchip (Figure 4.1) were fabricated using the elastomer Poly(dimethylsiloxane) (PDMS) (Sylgard 184, Dow Corning) and standard soft lithographic procedures (Whitesides 2001). The channel features were composed of a 30 μm thick SU-8 photoresist (MicroChem Corp, Newton, MA) patterned by diffused-light backside soft lithography onto a thin glass cover slip (Futai 2004). The

glass mold was placed in a dessicator under vacuum for 30 minutes with several drops of tridecafluoro-(1,1,2,2-tetrahydrooctyl)-1-trichlorosilane (United Chemical Technologies Inc., Bristol, PA) for ease of PDMS replica removal after molding. A thin layer of uncured PDMS (10:1 silicone elastomer: curing agent w/w ratio) was then spin coated (300 rpm for 2 minutes) onto the mold and left at room temperature for 12 hours. At this point, small neodymium magnets (1.5 mm-diameter, 0.5 mm-height, Engineered Concepts, Birmingham, AL) were placed on top of the channel regions and cured at 120° C for 1 hour. Uncured PDMS prepolymer was poured over the mold and cured at 60°C for 12 hours. The PDMS replica with inverse structures was then peeled off the mold. Holes of 2 mm diameter were bored into the PDMS for the reservoirs. This layer containing the negative relief channel features was irreversibly sealed to a 150 μm-thick layer of PDMS (formed by spin coating uncured PDMS onto a silanized glass slide and curing at 60°C overnight) by oxygen plasma treatment for 30 seconds (SPI Supplies, West Chester, PA, 10W, 300 mTorr). After oxidation, the surfaces were brought into conformal contact and placed in a 60°C oven for 5 minutes for irreversible sealing. The oxidation also rendered the surfaces hydrophilic, and to maintain hydrophilicity, the channels were immediately filled with phosphate buffered solution (PBS, Invitrogen). A complete chip is shown in Figure 4.1. The dimensions of the chip are 6 cm x 3 cm x 0.3 cm height. The rounded channels are 300 μm wide and 30 μm deep. The thin bottom spin coated layer is 150 μm thick. 5 areas of the chip were designated as immunoassay reaction sites, with each area supplied with fluid from 5 independent Braille pumps. The resulting device was aligned over the pins of a Braille display (Figure 4.1b,c).

Bead Functionalization

COMPEL Magnetic COOH modified microspheres (8.27 μm diameter) were coupled to the primary capture antibody (purified mouse anti-human IL-8) according to a modified version of literature protocol (Kellar 2001). Briefly 15 μl of a 5% bead solution was washed three times in PBS, then vortexed at medium speed at room temperature with 500 mg/ml of N-hydroxy-sulfosuccinimide (sulfo-NHS) and 1-ethyl-3-(3-dimethylaminopropyl)-carbodiimide hydrochloride (EDC) in PBS for 20 minutes. The bead sample was then washed 4 times with PolyLink coupling buffer, each time concentrating the beads in a microcentrifuge tube using an external magnet and removing the supernatant. Next 250 μl of the capture antibody (from 0.5 mg/ml stock) diluted into 1 ml of coupling buffer was added to the bead solution and allowed to react for 4 hours at room temperature with occasional mixing. The beads were then rinsed and resuspended in 100 μl of StartingBlock blocking buffer containing 0.02% sodium azide. After 30 minutes the beads were washed 3 times with PBS and resuspended in 250 μl of the blocking solution for storage at 4° C until use.

Apparatus for fluidic actuation

The immunoassay microsystem relies on fluid actuation provided from the movable pins of a commercially available Braille display located below the microchannels (Figure 4.1). The Braillex EL 40s Braille display (Papenmeier GmbH and Co. Schwerte, Germany) is used by the visually impaired to continuously read lines of computer text when attached through a USB cable to a computer with a screen reader program (HAL, Dolphin Computer Access, UK). A computer program written in Visual Basic was used to control the 40 Braille cells available, each with 8 independent pins (1.0

mm diameter). A device composed of a network of microchannels with flexible bottom membranes was aligned over the Braille pins. The pins in the upward position can valve specific regions of the bell-shaped channel for complete block of fluid flow. A specific sequence of three pins act as a pulsatile pump to guide fluid flow (Gu 2005).

This Braille actuation was used for the introduction of the solutions (beads, samples, and detection reagents) and for the washing buffer. In each case, the solutions were injected into the reservoirs prior to the experiment. Opening the valve and activating a series of three pins allowed the fluid to enter the reaction regions and interact with the beads.

Assay for Interleukin (IL)-8

Preparation of microchip

Microfluidic chips were filled with blocking buffer to prevent unwanted adsorption and placed in a humidified incubator overnight prior to use. After 24 hours, the device was aligned over the pins of the Braille display and the inlet reservoirs filled with washing buffer (0.1 M Tris buffer, 0.05% Tritin X-100, 0.05% Tween-20). The liquid was then pumped through for 10 min to wash the channels. After 10 min, the reservoirs were emptied, and each filled with 5 µl of the solution containing the antibody-coupled beads and pumped for 15 minutes. Following the bead loading, all reservoirs were cleaned with washing buffer three times prior to starting the assay.

Microfluidic assay

The sandwich assay for IL-8 was carried out using antibodies to IL-8 and a biotin/streptavidin-fluorophore linkage for detection. 5 µl standards (1-1000 ng/ml human IL-8) diluted in Starting Block blocking buffer (Pierce Chemicals, Rockford, IL)

as well as a control with no IL-8 was pipetted into the antigen inlet reservoirs. In a separate reaction, the detection antibody was created by mixing 20 µl of secondary antibody conjugated to biotin (100 µg/ml anti-human IL-8-biotin) and 20 µl of streptavidin/AlexaFluor 594 (100 µg/ml) for 10 minutes prior to the start of the assay. The washing buffer was introduced into the first reagent inlet. At the beginning of the assay 5 µl of the detection solution was pipetted into the first antigen inlet (containing the control sample) and pumped through the channel. After 10 minutes, another 5 µl of detection solution was introduced into the second inlet (containing the first IL-8 standard) and then pumped through. This was repeated on the remaining three channels. After 40 minutes elapsed, pumping was stopped in the first channel, and the washing buffer pumped through to the immobilized bead region to remove any excess antigen/antibody molecules. After 10 min, the first channel was valved off and the washing buffer pumped to the second channel. The last three channels were washed in a similar manner. This staggering was done due to the design of the device that has only a single inlet for introducing washing buffer into 5 channels. At the conclusion of the assay PBS was used to fill the channels and reservoirs to stop flow, and the chip removed from the Braille device and transferred to the microscope for imaging. A schematic illustration of the relevant immunocomplex formation is shown in Figure 4.2.

Bead imaging and data analysis

An inverted microscope (Nikon Eclipse TE2000 Inverted Microscope, Nikon, Tokyo) and a digital cooled CCD camera (CoolSNAP HQ2, Photometrics) operated with MetaMorph 6.3r7 image acquisition and analysis software (Molecular Devices, Downingtown, PA) were used to acquire pictures of the channels using a 40x water

immersion objective (Nikon). For fluorescence imaging, the microscope was equipped with a high pressure mercury lamp (Nikon) and filter cube G-2E/C to match the excitation and emission wavelengths (590/617) for the AlexaFluor 594 dye. From each image, the fluorescence intensity from random circular regions containing beads, as well as a region of background channel were measured using the MetaMorph software. Standard curves were generated by averaging the intensity values for each IL-8 concentration minus the background intensity.

Cell culture and stimulation

A549 cells (American Type Culture Collection, VA) were grown to confluence in a 100 mm diameter Petri dish in culture medium (Ham's F-12K with 10% fetal bovine serum, 1% penicillin/streptomycin, and 1% L-glutamine, Invitrogen). Prior to seeding, the PDMS reservoirs were filled with culture media and placed in the incubator overnight. The channels were valved off by placing the device over a thin wire attached to a glass slide to prevent the flow of media into the microchannels. The A549 cell monolayer was detached from the Petri dish using trypsin, transferred to a 15 ml conical and centrifuged to form a pellet. After removing the supernatant, the pellet was then resuspended in 4 ml of culture media and 10 μl of cell solution added to both of the cell culture inlet regions. The system was placed in an incubator for 12 hrs to allow for cell attachment. The cell culture media was then removed from the reservoirs, and 10 μl of serum free media (growth media minus the fetal bovine serum) was added to both inlets. The channels were still valved off to isolate the regions of cell attachment. After another 12 hrs, the media in one inlet containing cells was replaced with 10 ng/ml of TNF-α (Cell

Sciences, Canton, MA) in serum free media. After 15 hrs, the device was placed on the Braille device and the assay was carried out as detailed in the previous section.

4.3 Results and Discussion

Microfluidic immunoassays are fast becoming a powerful tool for molecular and cellular analysis as well as in clinical diagnosis. Microchips allow us to miniaturize systems with the advantages of speed, automation, and volume reduction. It is difficult to detect proteins in microchannels with such small volumes (10-100 nL) containing small amounts of molecules. To do so requires a sensitive, non-diluting assay. Immunoassay systems which involve microbeads coated with the primary antibody or antigen have many advantages including: high surface area to sample volume ratio, reduced diffusional distances, convenience of fluidic handling, and a high degree of synthetic flexibility. The increased surface area to volume ratio provides more binding sites for the analyte which can amplify the signal and enable the use of smaller volumes. The Luminex FlowMetrix System, for example, is a popular bead-based assay where polystyrene beads embedded with precise amounts of red and infrared dyes are coupled to the capture antibody. A green reporter dye is attached to the secondary detection antibody. Computer software and flow cytometry is able to separate the beads based on red/infrared, and then measure the amount of green fluorescence from each set. This system has the potential to measure up to 100 different cytokines simultaneously with a detection range less than 10-50,000 pg/ml for 6 cytokines (Martins 2002). However the Luminex flow analyzer is a complex benchtop instrument involving optoelectronic components that are bulky and expensive. Sheath fluid and a vacuum manifold with pump are also required to perform the microfluidic assay. Sato et al. have demonstrated a sandwich immunoassay on a

microchip fabricated with branching microchannels and weir structures to entrap the beads. In this system they were able to process up to 4 samples simultaneously with a reduced total assay time of 50 min (Sato 2002). However this system requires complicated chip fabrication, specialized detection, and can assay for only one antigen at a time. An alternative is to use magnetic beads trapped within the channels by an external magnetic field allowing for simpler washing steps and reuse of the system (Hayes 2001). Our device uses this latter approach.

Microchip design for magnetic bead capture

The use of paramagnetic microbeads as the substrate for the immunoassay is a key point of the microfluidic device. There are other available methods for incorporating magnetic elements within microfluidic systems (Choi 2000, Hayes 2000) with the most popular method being an external magnetic field applied to the channel region, for example through a rare earth magnet placed on top of the device (Hayes 2000). In our device, the paramagnetic beads are immobilized in the PDMS microchannels through small embedded magnets that are placed above the channel regions designated for cytokine immunoassays (Figure 4.1a). The advantage of using paramagnetic beads includes the ability to pack, position, and then remove the beads to reuse the system. We are also able to form a thin monolayer containing several beads (10-50) or a packed bed containing many beads (greater than 100). The number of beads trapped depends on several conditions including the initial concentration of bead solution, flow rate through the channel (controlled by the pumping speed) and the duration of flow. Since we measured the average fluorescence per bead in each microchannel and not the total

fluorescence intensity, is was unnecessary to rigidly control the number of beads per channel.

Fluidic control

Bulk flow in microchannels can be achieved through various methods such as external power sources for electroosmotic flow (Linder 2002), syringe pumps for pressure-driven flow (Sato 2002), capillary driven flow (Hosokawa 2005), and a mechanical rotator for centrifugation-induced flow (Lai 2004). The piezoelectically actuated pins of the Braille display described here provides unique fluid delivery capabilities as it allows for active and precise microfluidic control of reagent transport throughout the interconnected microchannel network. The flow rates in the channel can be controlled by altering the time in between the refreshable pin movements of the Braille device. Higher flow rates were used for washing the beads, while a slower flow rate was used for the incubation periods. Sequential introduction of samples, reagents, and buffers was performed using the Braille pins. Flow can also be stopped to allow for cell attachment or long incubation periods. Having multiple pins that pump at the same frequency for each channel also allows us precise control over the antibody and antigen quantities being delivered to the microbeads. The volume of the solution dispensed is defined by the volume of the channel and the pumping speed, thus eliminating the variability of pipetting.

Antibody concentrations

The density of active capture sites in an assay plays an important role in defining the maximum number of antigen molecules captured. Low concentrations do not provide enough capture sites for the antigens, thereby decreasing the sensitivity range of the

assay. On the other hand, excessive concentrations can reduce the capture efficiency, possibly due to steric effects that block access to the antigen epitopes in solution. The concentration of capture antibody covalently coupled to the microbeads was optimized prior to the assay. (Data not shown) Since the bead surface area was much smaller compared to the surface of 96 well plates, much less capture antibody was required.

IL-8 Immunoassay

Cytokines are regulatory proteins produced by different cells during the inflammatory response and are active at picomolar to femtomolar concentrations. The imbalances in the production of cytokines are often implicated in many disease states therefore the accurate detection and quantification of cytokine levels are crucial to studying the pathological process and their role in the immune system (Ao 2004). IL-8 is a chemokine (8kDa) that is a major mediator in the inflammatory response following injury. In our experiments, IL-8 was chosen as a cytokine that represents a low-abundance protein whose levels are of biological significance. IL-8 levels were determined by a bead-based sandwich immunoassay with fluorescence detection. By using a sandwich assay with beads, very small amounts of antigen can be captured effectively and selectively through the use of 2 recognition events between the antigen and 2 antibodies. Covalent attachment of the primary capture antibody was performed off chip using COOH surface activated microbeads. Prior to starting the assay, the beads were trapped in the microchannels (suspended by the magnet) and the antigen was in the antigen inlet reservoirs. Done off-chip was the incubation of the secondary antibody conjugated to biotin and the streptavidin/AlexaFluor 594 conjugate. The reaction of the primary antibody coated beads, the antigen (IL-8), and the secondary antibody-

AlexaFluor 594 conjugate was done inside the microchannels with an incubation time of 40 minutes. Residual nonspecific signals were minimized by optimization of washing times, blocking solution, primary antibody concentrations, and incubation times.

Figure 4.3 shows a standard calibration curve obtained for IL-8 using IL-8 standards diluted in A549 cell culture media. Background fluorescence measurements taken from the control (with no antigen present) is subtracted from all of the intensity measurements. The range of IL-8 detected was from 5 to 100 ng/ml. The averaging over multiple beads was necessary due to the variation of signal intensities within a channel. The range of IL-8 concentrations measured was limited by the amount of primary antibody covalently attached to the microbeads in the first step. The amount of capture antibodies bound to the microbeads was optimized as described above, however saturation occurred with fast and complete coverage of the binding sites at higher antigen concentrations. Sensitivities can be improved by either reducing the number of beads per assay thus concentrating the signal onto fewer beads, or by maximizing the signal by increasing the number of beads or amount of detection antibody.

Compared to 96 well plate formats, which require 150-250 μl of sample per well, this immunoassay reduces the sample consumption to less than 5 μl of antigen solutions. The assay is also relatively fast compared to large scale systems, eliminating the hours of incubation necessary for diffusion-limited reactions. The device is also amenable to batch fabrication with multiple replica molds formed in a short time easily and inexpensively. Rapid turnover time can be achieved since the microspheres were coupled to the capture antibody prior to the assay and can be replaced with fresh microbeads between assays.

The reproducibility of the assay was tested by repeating the experiment on 2 different days using the same IL-8 standards. Figure 4.4 shows the results of experiments using antigen concentrations ranging from 0 to 1000 ng/ml. In the second experiment, the order of the antigens was also reversed, with the control (0 ng/ml) in the channel on the very right, while the highest concentration was tested on the left channel.

The system can also be adapted to the determination of other analytes with the right selection of primary and secondary antibodies. Figure 4.5 shows the results of an assay to test for human IgG (Sigma) using goat anti-human IgG unconjugated coupled to the beads, and goat anti-human IgG conjugated to fluorescein (FITC) (Jackson ImmunoResearch Labs) as the detection antibody.

Measuring IL8 released from alveolar epithelial cells

A typical application for immunoassays is the detection of cytokines secreted by cells in culture stimulated by growth factors or other cytokines. The A549 cell line consist of alveolar epithelial type II cells that when stimulated by tumor necrosis factor (TNF)-α, are known to secrete inflammatory cytokines such as IL-8 (Standiford 1999). TNF-α is a pleiotropic factor that is capable of activating multiple signal transduction pathways and plays many roles in the generation and regulation of immune responses. Figure 4.3b shows the results of an assay in which A549 cells cultured in one of the antigen reservoirs were stimulated with 20 ng/ml TNF- α. After 15 hours the media was pumped through to the immobilized region for the assay measurement. Of the 5 available channels for the assay, 2 were used to culture cells (a control, and TNF-α stimulated cells), and the other 3 for IL-8 standards used to make the calibration curve. From the calibration curve, the amount of IL-8 released by the TNF stimulated cells was calculated

to be approximately 70 ng/ml. With an estimate of 1800 cells/reservoir (diameter of 3 mm), and 5 μl volume of media, we calculated that approximately 0.013 pg of IL-8 was released per cell per hour. This agrees with the value obtained by Standiford et al. with A549 cells stimulated in Petri dishes with 20 ng/ml TNF-α (Standiford 1999).

In this study, A549 alveolar epithelial cells were cultured in a PDMS well to obtain a larger surface area to volume ratio. The small cell numbers involved requires a highly sensitive, non-diluting immunoassay. Therefore, it is crucial to integrate an on-chip bead-based immunoassay system to detect and quantify the level of cytokines. The combination of a PDMS immunoassay chip and miniature PDMS cell culture well allows for a smaller overall size of the system with the required detection sensitivities. The use of microfluidics is beneficial in that it will facilitate sample acquisition, require only small volumes of samples, measure cytokines in a more concentrated solution, and allow for integrated assays on the cell culture device.

4.4 Conclusions

We have demonstrated a successful bead-based immunoassay system on a monolithic microfluidic chip controlled by a Braille display. This system provides a reliable means to measure the release of cytokines from chemically stimulated cells cultured on the microfluidic system. All processes of the assay: cell culture, chemical stimulation, assay reactions, and detection were integrated onto a single microchip. The microsystem described here is an ideal tool to monitor the by-products of cellular responses to chemical stimulation. The system is not limited to alveolar epithelial cells and can be applied to other cell types. In addition, with the appropriate reagents, the system can be used to assay for a variety of antigens. Multiple antigens simultaneously

can also be assayed for by slight modifications to the system design. Future work will focus on further automation of fluid delivery. The system is also amenable to highly parallel assays with further decreases in time and reagent consumption. The availability of a rapid, easy to use immunoassay system can have significant implications over a wide range of disciplines.

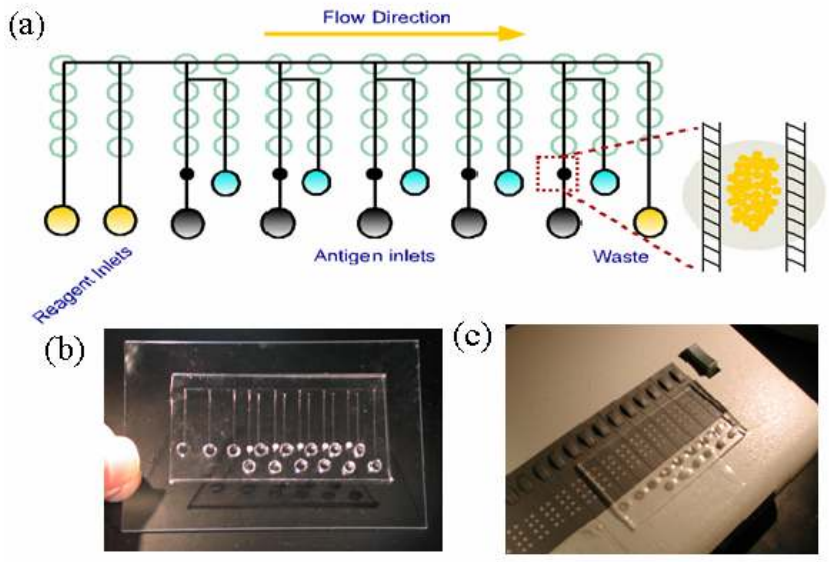

Figure 4.1: (a) Microchannel network used for immunoassay. Black dots: magnets, open circles: Braille pins, and colored circles: reservoirs. (b) PDMS immunoassay microchip placed over the pins of a Braille display (c).

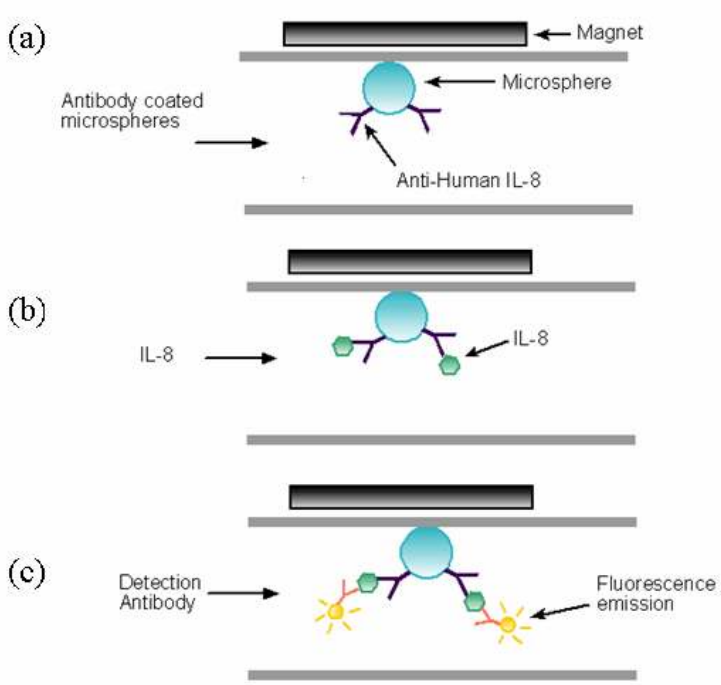

Figure 4.2: Steps for bead-based immunoassay. Side views of 30 μm high microchannel with 8 μm diameter microspheres. (a) Paramagnetic microspheres precoated with capture antibody are pumped into microchannels and captured using embedded magnet. (b) Primary antibody is flowed through the system and detection is done with a secondary antibody coupled to a fluorophore (c).

(a)

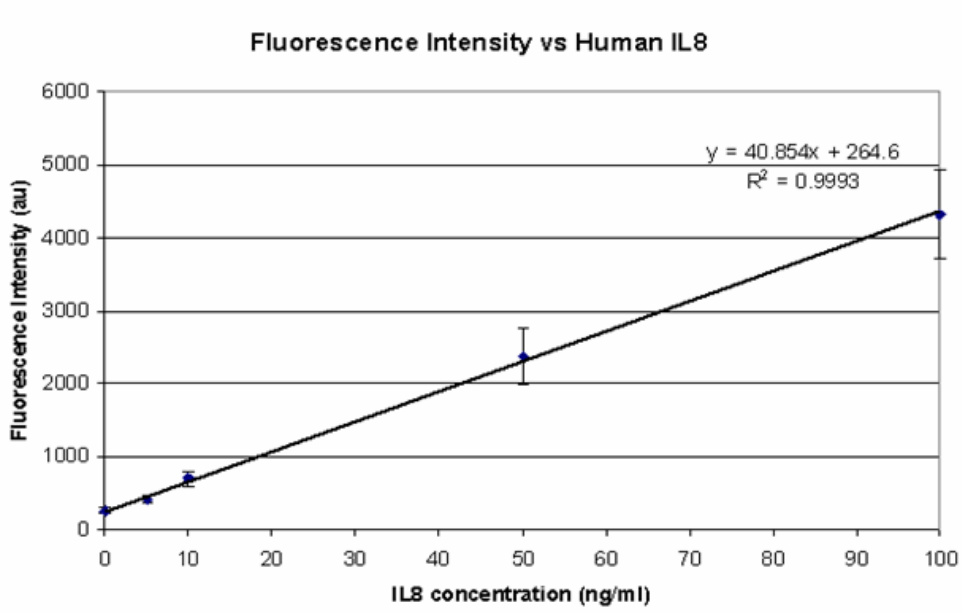

(b)

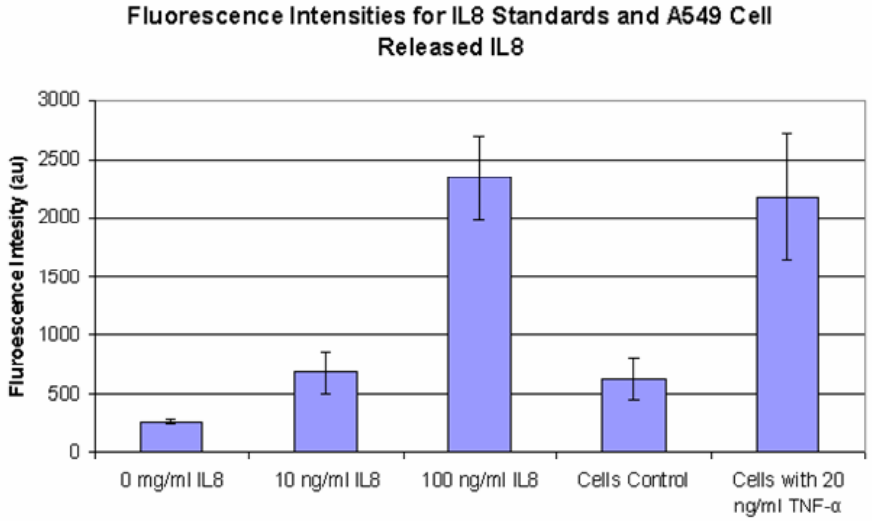

Figure 4.3: (a) Fluorescence intensities for each IL-8 concentration. Results are presented as average fluorescence intensities taken from random regions of beads. (b) Fluorescence intensities taken from 3 standard concentrations of IL-8, one control with cells, and one from cells stimulated with 20 ng/ml TNF-α.

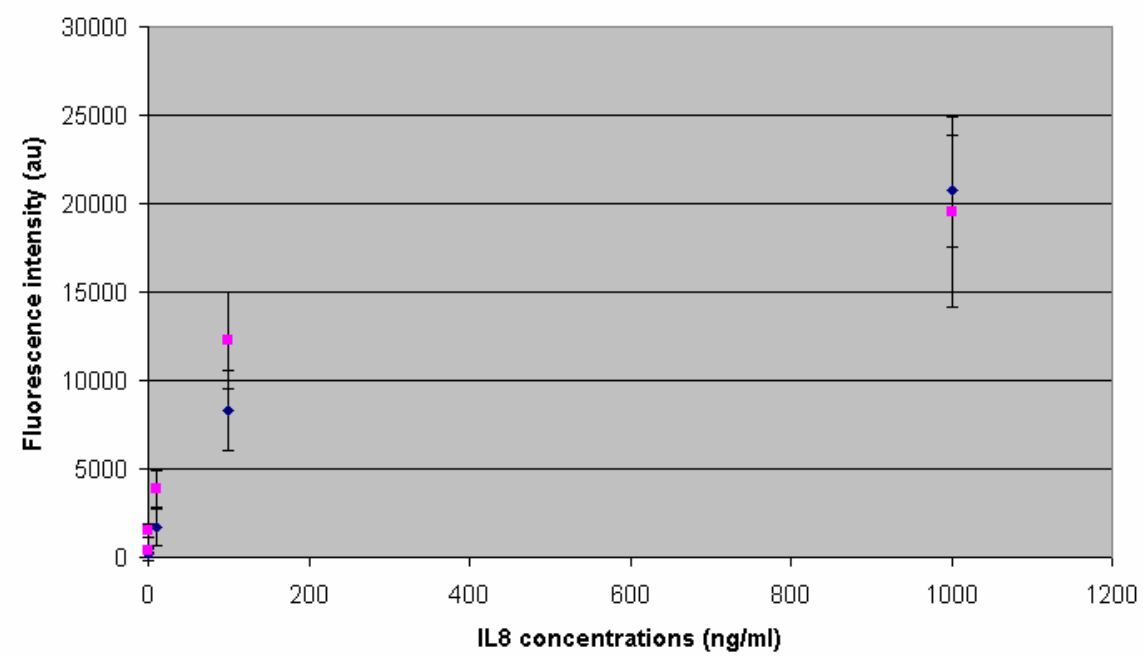

Figure 4.4: Test for reproducibility of system. Average fluorescence intensities obtained from two sets of experiments using IL-8 antigen concentrations ranging from 0 to 1000 ng/ml.

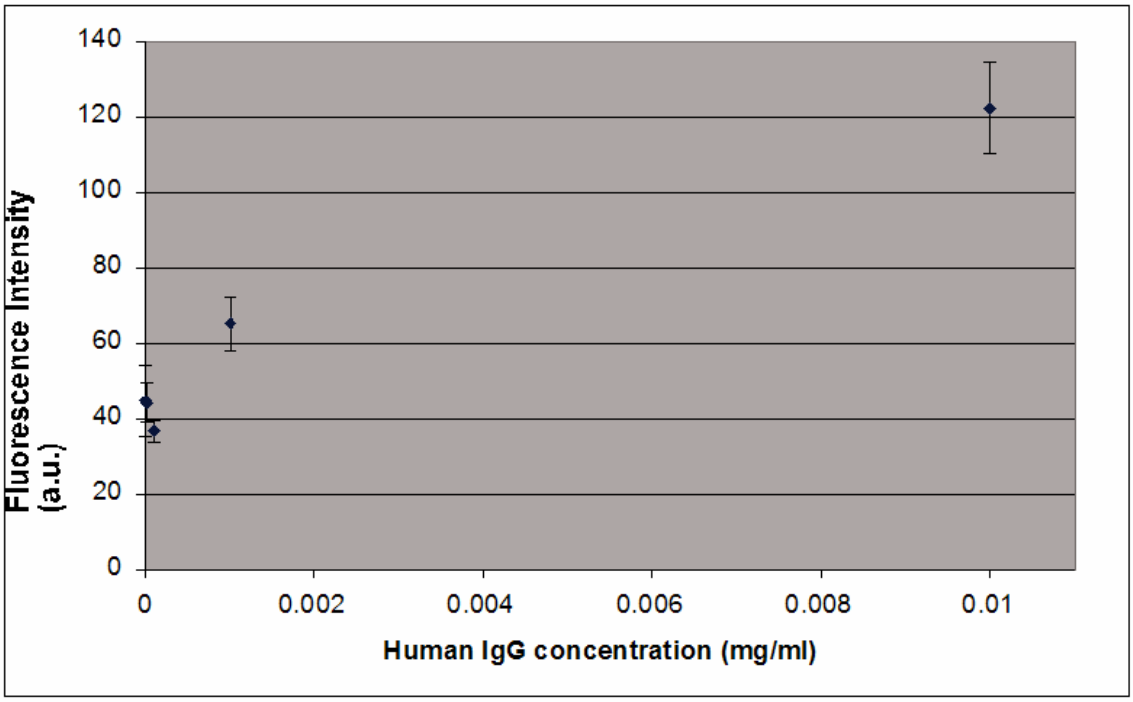

Figure 4.5: Average fluorescence intensities from experiments done using human IgG as the antigen.

4.5 References

Abdel-Hamid I, Atanasov P, Ghindilis AL, Wilkins E. Development of a flow-through immunoassay system. Sensors and Actuators B. 49, 202-210. 1998.

Ao X, Sellati TJ, Stenken JA. Enhanced microdialysis relative recovery of inflammatory cytokines using antibody-coated microspheres analyzed by flow cytometry. Anal. Chem. 76, 3777-3784. 2004.

Choi JW, Oh KW, Thomas JH, Heineman WR, Halsall HB, Nevin JH, Helmicki AJ, Henderson T, Ahn CH. An integrated microfluidic biochemical detection system for protein analysis with magnetic bead-based sampling. Lab on a Chip. 2; 27-30. 2002.

Eteshola E, Leckband D. Development and characterization of an ELISA assay in PDMS microfluidic channels. Sensors and Actuators B. 72, 129-133. 2001.

Eteshola E, Balberg M. Microfluidic ELISA: On-chip fluorescence imaging. Biomedical Microdevices. 6(1), 7-9. 2004.

Futai N, Gu W, Takayama S. Rapid prototyping of microstructures with bell-shaped cross-sections and its application to deformation-based microfluidic valves. Adv. Materials. 16: 1320+ 2004.

Gu W, Zhu X, Futai N, Cho BS, Takayama S. Computerized microfluidic cell culture using elastomeric channels and Braille displays. PNAS. 101(45); 15861-15866. 2004.

Hatch A, Kamholz AE, Hawkins KR, Munson MS, Schilling EA, Weigl BH, Yager P. A rapid diffusion immunoassay in a T sensor. Nature Biotech. 19, 461-465. 2001.

Hayes MA, Polson NA, Phayre AN, Garcia AA. Flow-based microimmunoassay. Anal Chem. 73, 5896-5902. 2001.

Hosokawa K, Omata M, Sato K, Maeda M. Power-free sequential injection for microchip immunoassay toward point-of-care testing. Lab on a Chip. 6; 236-241. 2006

Inoue I, Wakamoto Y, Moriguchi H, Okano K, Yasuda K. On-chip culture system for observation of isolated individual cells. Lab on a Chip. 1, 50-55. 2001.

Jiang X, Ng JMK, Stroock AD, Dertinger SKW, Whitesides GM. A miniaturized, parallel, serially diluted immunoassay for analyzing multiple antigens. J. Am. Chem. Soc. 125, 5294-5295. 2003.

Kellar KL, Kalwar RR, Dubois KA, Crouse D, Chafin WD, Kane BE. Multiplexed fluorescent bead-based immunoassays for quantitation of human cytokines in serum and culture supernatants. Cytometry. 45, 27-36. 2001.

Lai S, Wang S, Luo J, Lee LJ, Tang ST, Madou MJ. Design of a compact disk-like microfluidic platform for enzyme-linked immunosorbent assay. Anal. Chem. 76, 1832-1837. 2004.

Linder V, Verpoorte E, de Rooij NF, Sigrist H, Thormann W. Application of surface biopassivated disposable poly(dimethylsiloxane)/glass chips to a heterogeneous competitive human serum immunoglobulin G immunoassay with incorporated internal standard. Electrophoresis. 23, 740-749. 2002.

Martins TB, Pasi BM, Pickering JW, Jaskowski TD, Litwin CM, Hill HR. Determination of cytokine responses using a multiplexed fluorescent microsphere immunoassay. Am J Clin Pathol. 118, 346-353. 2002.

Sato K, Yamanaka M, Takahashi H, Tokeshi M, Kimura H, Kitamori T. Microchip-based immunoassay system with branching microchannels for simultaneous determination of interferon-γ. Electrophoresis. 23, 734-739. 2002.

Schweitzer B, Wiltshire S, Lambert J, O'Malley S, Kukanskis K, Zhu Z, Kingsmore SF, Lizardi PM, Ward DC. Immunoassays with rolling circle DNA amplification: a versatile platform for ultrasensitive antigen detection. PNAS. 97 (18), 10113-10119. 2000.

Schweitzer B, Roberts S, Grimwade B, Shao W, Wang M, Fu Q, Shu Q, Laroche I, Zhou Z, Tchernev VT, Christiansen J, Velleca M, Kingsmore SF. Multiplexed protein profiling on microarrays by rolling-circle amplification. Nature Biotech. 20, 359-365. 2002.

Shackman JG, Dahlgren GM, Peters JL, Kennedy RT. Perfusion and chemical monitoring of living cells on a microfluidic chip. Lab on a Chip. 5, 56-63. 2005.

Standiford TJ, Kunkel SL, Basha MA, Chensue SW, Lynch III JP, Toews GB, Westwick J, Strieter RM. Interleukin-8 gene expression by a pulmonary epithelial cell line. J. Clin. Invest. 86, 1945-1953. 1990.

Unger MA, Chou H-P, Torsen T, Scherer T, Quake S. Monolithic microfabricated valves and pumps by multilayer soft lithography. Science. 288, 113-116, 2000.

Whitesides GM, E. Ostuni, S. Takayama, X. Y. Jiang and D. E. Ingber, Soft lithography in biology and biochemistry, Annu. Rev. Biomed. Eng., 3: 335-373, 2001.

Yeung WSB. Luo GA, Wang QG, Ou JP. Capillary electrophoresis-based immunoassay. J. of Chromatography B. 797, 217-228. 2003.

Chapter 5

Fabrication of Microfluidic Mixers and Artificial Vasculatures using a High-brightness Diode-pumped Nd:YAG Laser Direct Write Method

This paper describes a direct write laser technology, which is fast and flexible, for fabricating multiple-level microfluidic channels. A high brightness diode-pumped Nd-YAG laser with slab geometry was used for its excellent beam quality. Channels with flat walls and staggered herringbone ridges on the floor have been successfully fabricated and their ability to perform passive mixing of liquid is discussed. Also, a multi-width multi-depth microchannel has been fabricated to generate biomimetic vasculatures whose channel diameters change according to Murray's law, which states that the cube of the radius of a parent vessel equals the sum of the cubes of the radii of the daughters. The multi-depth architecture allows for flow patterns to resemble physiological vascular systems with lower overall resistance and more uniform flow velocities throughout the network compared to planar patterning techniques which generate uniformly thin channels. The ability to directly fabricate multiple level structures using relatively straightforward laser technology enhances our ability to rapidly prototype complex lab-on-a-chip systems and to develop physiological microfluidic structures for tissue engineering and investigations in biomedical fluidics problems.

5.1 Introduction

Over the last decade, there has been a tremendous growth in the need to fabricate three-dimensional (3D) multi-level microstructures for microfluidic systems as tools for chemistry and biochemistry, optical elements, tissue-engineering scaffolds, and other applications. Most micro-device construction takes advantage of technologies established in the microelectronics field, such as photolithography and etching of silicon substrates (Madou 2002), to fabricate electronic controls, to generate channel features, and to prepare master molds for creating polymeric microchannels. However, conventional photolithography often limits the flexibility and size of fabrication. For example, photolithography requires photomasks that are expensive and time consuming to fabricate, for every new structure or pattern to be generated. In device development where frequent redesign of components is inevitable, this adds tremendously to the cost and time required for fabrication. In the case of 3D, multi-level microfabrication, the time and cost of fabrication are further increased by the need for multiple masks and multiple steps with alignment between the different levels to create each structure. In this paper, we describe a faster and more flexible alternative method to fabricate multiple-level microfluidic channels using maskless laser direct micromachining. Although a variety of materials can be machined using lasers, here we focus particularly on fabrication of silicon structures because it is a commonly used material for microfluidics that has the following three advantages: (i) Good thermal conductivity and low thermal capacity, thereby allowing fast thermal cycles and high thermal gradient between adjacent areas. (ii) Robust materials properties that allow use in applications that require strong solvents, high temperatures, or chemically stable surfaces (Beebe 2002) (iii) The ability to

integrate electronic controls on the same substrate as the microfluidic device for lab-on-a-chip or micro-total-analysis-systems (μ-TAS) (Abramowitz 1999, Feldstein 1999, Legge 2002). Furthermore, silicon can also be used as molds for generating polymer microfluidic systems.

A number of techniques have previously been developed to overcome the 3D fabrication limitations of standard photolithography. For example, a variety of gray scale masks that can vary the amount of exposure received by photoresist have been used to create multi-level structures. Ultra-high resolution half-tone transmission photomasks have been used to generate 3D structures (Wagner 1995). Chen *et al.* (Chen 2003) have developed "microfluidic photomasks" (μFPMs) in which gray scales are produced by changing the concentration of light-absorbing dye flowing through microfluidic channels. In another technique, an extra post-processing microstereolithography step, allows for the building of complex, 3D polymer structures (Bertsch 1999). Planar processes such as thin films and bulk silicon etching using scanning lasers are used to create these microstructures. Other techniques include micromirror projection displays (Sampsell 1994), high-energy beam-sensitive glass photomasks, metal-on-glass photomasks (Däschner 1995) and 3D direct-write assembly of a fugitive organic ink (Therriault 2003). Although these methods are useful, they have limitations such as high costs and complicated procedures (Chen 2003, Däschner 1995, Therriault 2003), allowing for only a few gray-scale levels (Däschner 1995), requiring preparation of photomasks, or having limitations in the types of patterns generated (Chen 2003).

Lasers have long been successfully employed in many areas for micromachining (Bäuerle 1996, Gower 2000, Knowles 1998, Shirk 1998). The advantages are that no

mask is required and any redesigns can be easily achieved by changing the program that controls the x-y machining stage. In addition, a high degree of accuracy and consistency can be achieved. In general, laser micromachining is a material removal process where the substrate (workpiece) is exposed to laser energy which ablates off material in specified areas until the final desired shape is achieved. Although the shorter pulse lasers such as the picosecond and femtosecond lasers are often highlighted as the new generation precision micromachining tool, nanosecond lasers such as the excimer and Q-switched Nd:YAG lasers are still the most commonly available ones. This is because the nanosecond lasers provide the shortest pulse length possible without use of complex and expensive equipments. Of these two types of nanosecond lasers, the excimer laser ─due to its poor beam quality─ is generally used for fabrication by mask projection methods whereby a mask is imaged onto a substrate (Rizvi 2002, Harvey 1995). The fabrication of the mask not only adds extra cost and time to the process, it is also not suitable for prototyping since any design changes require a new mask. Although in the recent years, companies (such as Resonetics, Potomac, etc) are able to provide direct writing with the excimer laser in some situations, they are typically limited to very fine resolution machining. Additionally, due to its shorter wavelength, energy absorption occurs near the surface (Benavides 2001, Klotzücher 2002) of the substrate which results in smaller penetration depth. As such, this makes the excimer laser inefficient to machine microdevices which are on the order of hundreds of microns due to the long machining time needed. On the other hand, Q-switched Nd:YAG lasers generally have much better beam quality and are able to focus more tightly to enable more rapid material removal. The Nd:YAG lasers can also be frequency converted from the fundamental 1064 nm

wavelength to 532 nm, 326 nm and 266 nm by using non-linear crystals. The high beam quality and the variable wavelengths capability of the Nd:YAG laser enables a wider range of materials to be machined because the properties of the laser beam can be better tailored to match the adsorption characteristics of the different substrates. In this paper, we take advantage of these favorable properties of the diode-pumped Nd:YAG laser to perform maskless fabrication of microchannels in silicon. We demonstrate the flexibility and versatility of this fabrication strategy by creating microchannels with ridges or multiple depths for biochemical microfluidics applications (Figure 5.1).

5.2 Methods

Fabrication

The laser used for micromachining the micro-channels was the TRW (DP-11) risk reduction, high-brightness diode-pumped Nd:YAG slab laser manufactured by Northrop Grumman (known formerly as TRW). It has an exceptional high beam quality (1.3-1.7X Diffraction Limit) with options for frequency doublings. The detailed characteristics of the laser and its performance are well described elsewhere (Machan 1996). With the laser's high beam quality and exceptional brightness, various precision machining procedures have been successfully demonstrated. In this study, the laser was set to operate at its fundamental wavelength of 1064 nm, repetition rate of 200 Hz and pulse width of 150 μs (duty cycle of 3%). The laser beam was further modulated by an acousto-optic modulator with each spike having a 75 ns full width half maximum (FWHM) at a period of 7 μs with a duty cycle of 80%. A half-waveplate was used to vary the average power from the laser in order to achieve different ablation rate without changing the laser setting, while a quarter-wave plate was used to circular polarize the final processing

beam. (Figure 5.1a). For the chaotic mixer, the laser average power was set to 1 W, while for the 4 level multi-width multi-depth microchannel, the laser average power was set to 0.78 W for the 1st branch, 0.6 W for the 2nd branch, 0.55 W for the 3rd branch and 0.5 W for the 4th branch. On the other hand, the laser average power, for the 8 level multi-width multi-level microvasculature network microchannels, was set from a range of 0.5 W for the 8th branch to 3 W for the 1st branch. All the processes were carried out in air.

When the laser beam is at its focus, the shape is near-Gaussian, with a symmetric diffraction spot pattern surrounding a bright central lobe (Figure 5.1b). For precision micromachining, these diffraction spots surrounding the bright central lobe are filtered off by a spatial filter. The resulting beam passing through the spatial filter to the workpiece will be a clean-cut symmetric near-Gaussian beam.

An N-type <100> 660 μm thick silicon wafer was first sliced into the required dimension using a diamond blade glass cutter. Computer Numerical Control (CNC) codes were programmed to control the movement of the X-Y stage based on the desired channel dimensions/patterns. The microchannel was then machined by exposing the laser beam directly onto the wafer. By changing the increment step movement of the X-Y stage table the amount of laser beam overlap can be adjusted, resulting in changes in the amount of material being ablated. As shown in Figure 5.2, if the amount of overlap is insufficient, there will be too much un-ablated material. On the other hand, if the amount of overlap is too excessive, the structures will be over ablated. By optimizing the amount of the laser beam overlap, we are able to generate staggered herringbone structures on the floor of microchannels.

In general, it is difficult to micromachine silicon using nano-second pulse ("long" pulse) lasers due to the strong thermal effect on silicon. Some of these effects are larger heat affected zones (HAZ), appearance of microcracks, and formation of recast and melt layers that consist of solidified silicon melt and silicon oxide (SiO_2). As such, there are few successful reports on the use of long pulse lasers for silicon micromachining. We overcame the problem of debris buildup by adapting methods of Dauer *et. al.* who removed solidified oxide and silicon melt by wet chemical etching in 40 % HF for 10 mins at a rate of 60 μm/min followed by 30 % KOH at 70 ^{o}C for 10 mins at a rate of 30 μm/hr along the <100> plane (Dauer 1999). It was noted that HF only removed silicon oxides while KOH removed any silicon melt created during laser machining and have little effects to the overall design of the microdevices (at most an additional 5 μm due to the KOH etching).

5.3 Applications

To demonstrate the usefulness of the technique we fabricated two types of channels of biochemical significance and interest that are time-consuming and costly to fabricate using conventional fabrication techniques due to multiple-mask requirements and multiple-step procedures: (i) the fabrication of a chaotic mixer which has ridges incorporated into microfluidic channel structures, and (ii) a multiple depth vasculature channel system with four or eight generations of channels that obey Murray's law.

Chaotic Mixer

Mixing is a crucial procedure for many biochemical processes. Mixing in microfluidic channels, however, is slow because flows in small channels are characterized by low Reynolds number (*Re*), in which the flow is laminar and uniaxial,

hence mixing occurs only by diffusion. For such uniaxial flows, mixing distances can be very long. Efforts to reduce this mixing length have led to the development of several micro-mixers. Many of these mixers (Schwesinger 1996, Koch 1998, Branebjerg 1996, Bessoth 1999) utilize flow splitting techniques, whereby incoming fluid is split into several narrower streams and rejoined together after mixing is complete. A more effective method to reduce the mixing length is to introduce transverse flows in microchannels (Johnson 2002, Stroock 2002) whereby slanted ridges at a 45 degree angle are placed on the floor of the channel. With the success of this design in generating transverse flows in microchannels, Stroock *et. al.* (Stroock 2002) further developed a "chaotic" micro-mixer, known as the staggered herringbone mixer (SHM), in which a series of diagonal ridges are etched onto the channel floor to further improve the mixing efficiency. Each ridge is placed at an oblique angle with respect to the long axis of the channel and the direction of symmetry of the channel switches at 1/3 times the width of the microchannel. Incoming fluid is subjected to a repeated sequence of rotational and extensional local flows by varying the orientation of the herringbones between half cycles, thus decreasing the time (distance) for complete mixing to occur. One of the challenges of using the SHM in microanalysis systems is the requirement to use multiple steps of photolithography to generate the structures; a first layer of photolithography to define the channel structure, followed by a second layer to define the pattern of the ridges. The patterns of ridges generated in the second layer must be carefully aligned onto the channel structures formed in the first step to form an effective mixer.

Here, we demonstrate the use of laser direct write to create the microchannel feature and the ridge features on the floor of the channel in one step. In order to test and

observe the laser-fabricated SHM for its mixing ability, a thin slab of optically transparent poly (dimethylsiloxane) (PDMS) was placed over the laser micromachined silicon wafer to generate a closed channel system. Reservoirs were attached onto the PDMS at the inlet while tubing was attached to the outlet and subsequently connected to a syringe pump. The device was then plasma oxidized for 7 minutes to make the channels hydrophilic, thereby improving the liquid flow inside the channels. An 80% glycerol-20% water solution and an 80% glycerol-20% water solution with fluorescent 1% bovine serum albumin (BSA) were prepared and injected into the inlet reservoirs, while a syringe pump pulled liquid at a rate of 1.4 mL/hr at the outlet. These highly viscous solutions and high molecular weight fluorescent probes, which result in lower apparent diffusion coefficients of molecules compared to those in water using small molecules were used to ensure a more stringent test for mixing.

Figure 5.3(a) shows SEM images for the channel with staggered herringbone ridges on the floor fabricated by laser direct micromachining while Figure 5.3(b) shows the flow images and their corresponding fluorescence intensity distributions. Although the herringbone structures are not as exact as those obtained from standard multiple-step photolithography, it is clear from Figure 5.3(b), that the multi-level structures generated by the one-step laser write technique is functional. For the channel with flat walls and floors (Figure 5.3(b) left), mixing hardly occur, with the two solutions simply flowing parallel side by side along the channel with little mixing. This is also manifested in the fluorescence intensity curve taken at the outlet of the channel, which shows fluorescence to be confined mostly to one half of the channel. On the other hand, the channel with the laser machined staggered herringbone ridges (Figure 5.3(b) right) provided a more

uniform fluorescence intensity across the channel, indicating greatly enhanced mixing efficiency as compared with the flat channel.

Artificial Vascular Networks

One of the important uses of microchannels is their use as artificial vascular networks to study the effect of fluid dynamics on cell response (Aunins 2003, Ma 2002, Gray 2002) to perform biomedical imaging research (Hitt 1999, Chen 1999, Yoshimura 2003), and to deliver oxygen and nutrients to cells within engineered tissue constructs (Borenstein 2002). Recreating microfluidic systems that generate physiological flow patterns in terms of fluid velocities, resistances, and flow bifurcation patterns is critical for obtaining physiologically relevant results in these studies and applications. Efficient fluid flow with minimal resistance and distribution to large areas becomes especially important when engineering tissues such as the liver, kidney, and the heart with inherently high metabolism, where a lack of oxygen and nutrients will lead to rapid death of cells. There have been a number of efforts to overcome these problems with microfabricated artificial vasculature networks. Most previous microfabrication efforts used photolithography to generate master molds (Borenstein 2002), where a model network of "blood vessels" is printed with a microfluidic design that starts from a single channel that branches out multiple times into thinner and thinner channels. The inherently 2-D nature of photolithography, however, results in microfluidic channels with uniform depth that generates non-physiological flow conditions and high flow resistances (Borenstein 2002).

A more physiological vascular network would be obtained through microfabrication of fluidic channels that obey Murray's law. In 1926, Murray discovered

a characteristic of vascular networks, now called Murray's law that minimizes the cost function, which is the sum of the friction power loss and the metabolic energy proportional to blood volume (Murray 1926). Murray's law describes the optimal condition for a vascular bifurcation whereby the cube of the radius of a parent vessel equals the sum of the cubes of the radii of the daughters. To date, Murray's law provides one of the closest approximations of a physiological vascular artery network.

In contrast to conventional photolithography, the laser-mediated direct micromachining technique described in this paper is able to generate multi-width and multi-depth artificial vasculatures straightforwardly (Figure 5.4). Multi-depth fabrication by laser is a direct, one step process that is fast to achieve because different depths can be generated simply by varying the setting of the half-wave plate to change the average power from the laser used to micromachine the channels (Figure 5.1). By creating channels with different depths, fluidic networks are obtained that obey Murray's law across multiple branching generations. The multi-depth channels better mimic physiological flow patterns with lower overall flow resistances and more gradual changes in the flow velocities across different generations of branching compared to channels of uniform depth (Figure 5.4).

Figure 5.4 compares two four-generation branching network systems - one which is planar and does not obey Murray's Law and another that does and was fabricated by direct laser micromachining. The differences in fluorescence intensity levels within the channel that obeys Murray's law (Figure 5.4d) is indicative of depth differences in different branching generations of the fluidic system and contrasts with the uniform fluorescence intensity seen in the flat channel (Figure 5.4c).

A simple test to visualize flow velocities and to mimic the flow of cells in blood was performed using fluorescent microbeads. Figure 5.4(e-f) shows histograms of average velocities of microbeads pumped through the two channels. The graphs show how the fluid flow velocities in the planar branching channel varies greatly between different branch generations whereas the velocities are less variable in the channel designed according to Murray's law (Figure 5.4e,f). This analysis confirms differences in particle flow characteristics between uniform-depth and multi-depth channels that obey Murray's law across multiple branching generations. To further demonstrate the capabilities of our laser direct write technique, an eight level vasculature system (Figure 5.5) was fabricated where the branching patterns not only obeyed Murray's law but also more closely mimicked the ability of the natural vasculature to efficiently distribute fluid to a large area. The large-area distribution capability is important because any artificial vascular system used for tissue engineering must be designed to support sufficient mass transport of nutrients and oxygen to cells in all areas of a construct, while avoiding high pressures and exposure of the cells to excess shear stresses. Biomimetic, multi-depth fluidic systems that obey Murray's law are expected to be useful in this regards because of lower resistances, slower average fluid velocities, and less shear generation. For example, assuming a simple rectangular cross-sectional geometry, the theoretical fluid flow resistance of the eight level channel design that obeys Murray's law (Figure 5.5) is calculated to be 33 times lower than that of the corresponding uniformly thin eight generation branching channel. Relatively small differences in depths of channels can contribute to large differences in overall fluid flow resistance because resistance in rectangular channels scale as height cubed.

Although we have only demonstrated fabrication of relatively simple four and eight generation branching structures with a focus on multi-depth channels, our laser direct write method is flexible and capable of generating virtually any type of branching patterns or numbers of branching generations. The patterns that can be generated are limited only by the range of the XY stage (the current system has a X range of ± 30cm and a Y range of ± 30cm), the size of the substrate, and by the spot size of the laser beam (approximately 100 μm diameter). In addition to the convenience of one-step fabrication, the ability to pattern over large areas maybe especially useful for tissue engineering applications where a large mass of cells need to be supported by an efficient vascular network. Given that the sizes of mammalian cells are generally on the order of 5-100 micrometers, the resolution achieved by our laser microfabrication technique is ideal for development of microfluidic systems that manipulate, culture, or analyze cells.

5.4 Conclusion

It is challenging to fabricate 3D multi-level microstructures using conventional microfabrication technologies such as photolithography and etching. Multiple exposure and alignment steps required by conventional techniques often limit the flexibility and size of the fabrication. A novel technology based on the readily available and easy to operate diode-pumped Nd:YAG laser has been employed successfully to micromachine multi-level microchannels on silicon wafers for microfluidic applications. This fabrication method allows flexibility in design changes and experimental trials making it useful for rapid prototyping. We demonstrate the versatility of the technology by performing one-step fabrications of a microfluidic mixer that has staggered herringbone structures and artificial vasculatures that have multi-width multi-depth structures and

obeys Murray's Law. The staggered herringbone structure generated by laser fabrication achieved rapid mixing of liquids as determined by fluorescence imaging. The multi-depth artificial vasculature allows more physiological flow patterns to be generated compared to uniformly thin channels and are expected to be advantageous for *in vitro* cell studies, for development of phantoms for biomedical imaging studies, and for tissue engineering applications where efficient transport of oxygen and nutrients is required. The versatility of this laser direct write micromachining technology is promising for lab-on-a-chip development and other biotechnology applications.

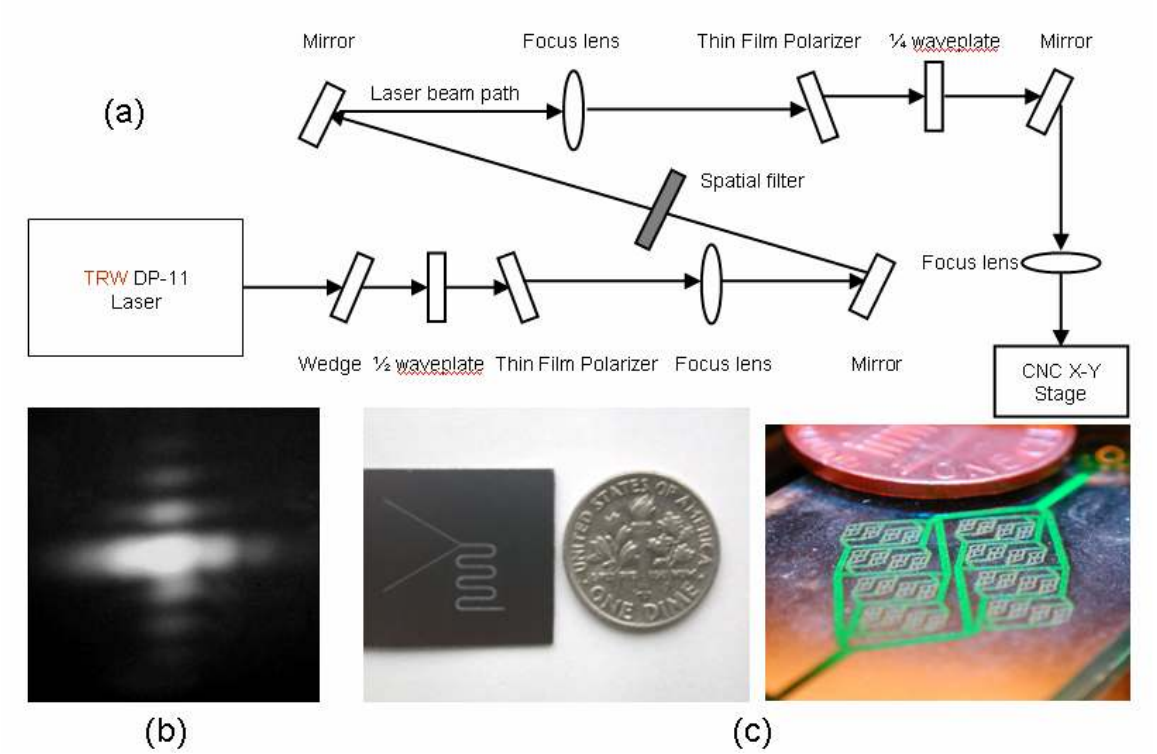

Figure 5.1: (a) Schematic view of a TRW DP-11 optical setup. (b) Laser beam at its focus with a symmetric diffraction spot pattern surrounding a bright central lobe before spatial filter. (c) Examples of fabricated microchannels. Left: Staggered herringbone mixer. Right: 8 level multi-width multi-level microvasculature network microchannels.

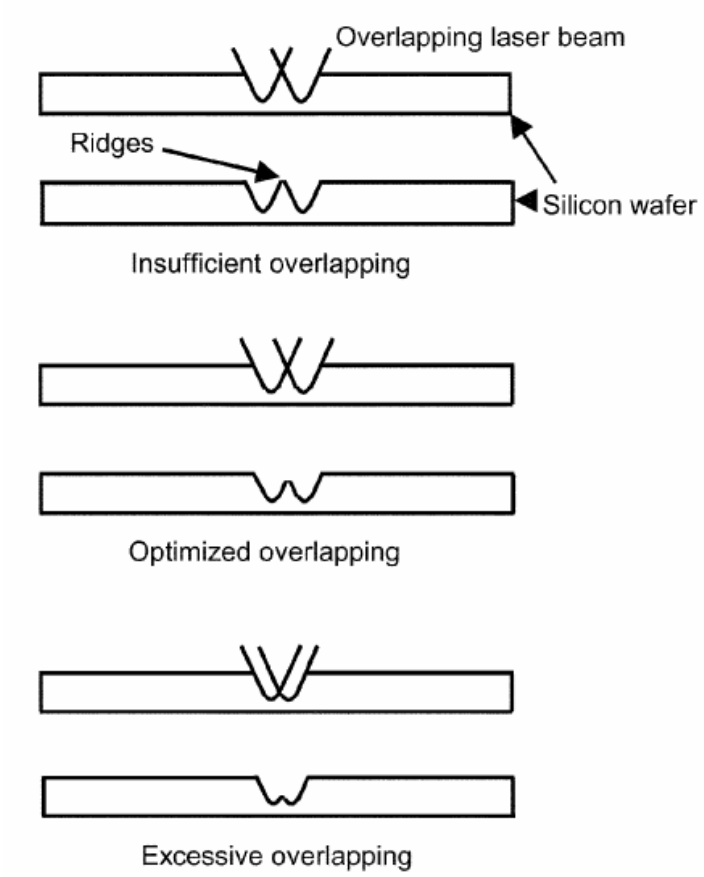

Figure 5.2: Schematic sketch to illustrate how the amount of beam overlapping determines the structures created. Top sketches represent the amount of overlapping of the laser beam while the bottom sketches represent how the amount of overlapping determines the shape of the ridges created.

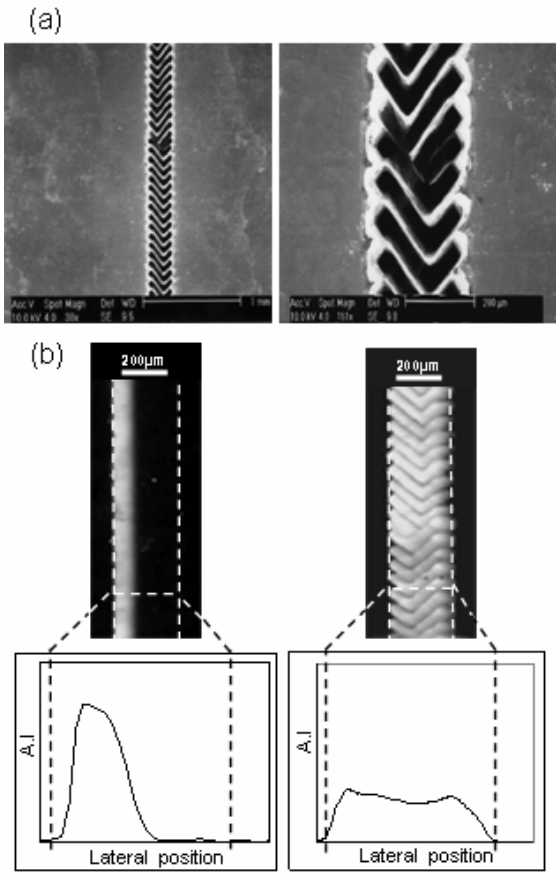

Figure 5.3: (a) Left: SEM image of staggered herringbone mixer viewed from the top. Right: Close-up SEM image. (b) Top: Fluorescent images viewed from the top of (left) flat walls channel (right) SHM. Bottom**:** Intensity curve versus lateral position across the channel taken at the outlet of the channel for the channel with (left) flat walls and (right) SHM. Both channels were pulled by a syringe pump at a rate of 1.4 mL/hr at the outlet.

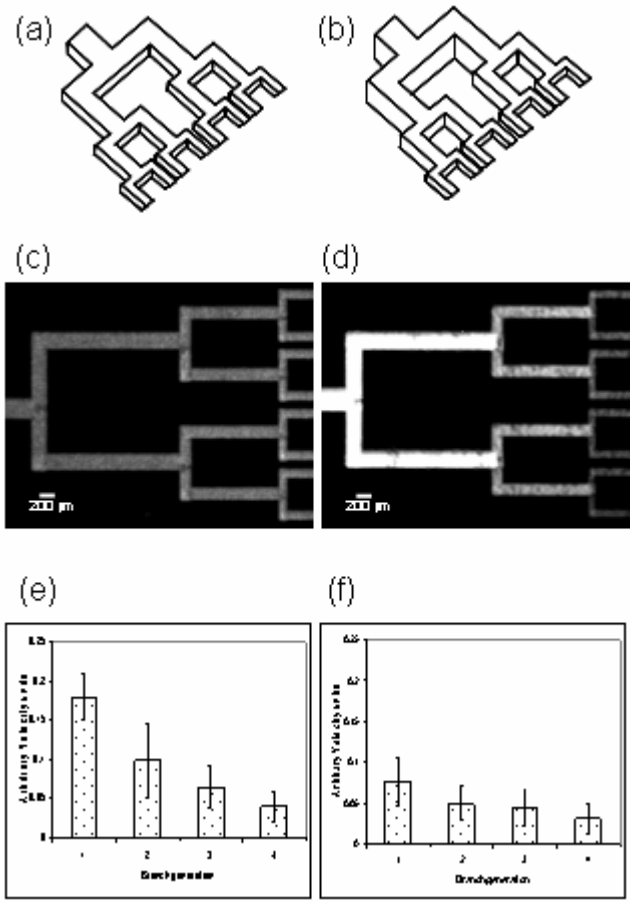

Figure 5.4: (a) Schematic sketch of the left half of the laser micromachined artificial vasculature system, which does not obey Murray's Law: flat channel (widths of 250, 200, 160, 125 μm; uniform depth of 125 μm). (b) Schematic sketch of the left half of the laser micromachined artificial vasculature system which obey Murray's Law: multi-depth channel (widths and depths are equal and are 250, 200, 160, 125 μm). To simplify fabrication, the shape of the channels cross section were designed to be square rather than circular for the present studies. (c) Image showing intensity levels corresponding to flat channel (d) Image showing the difference in intensity levels corresponding to different channel's depth. This illustrates how the multi width/depth channel obeys Murray's law. Histograms of average velocities of fluid pumped through the (e) flat channel (f) multi width/depth channel as determined by tracking of fluorescent microbeads.

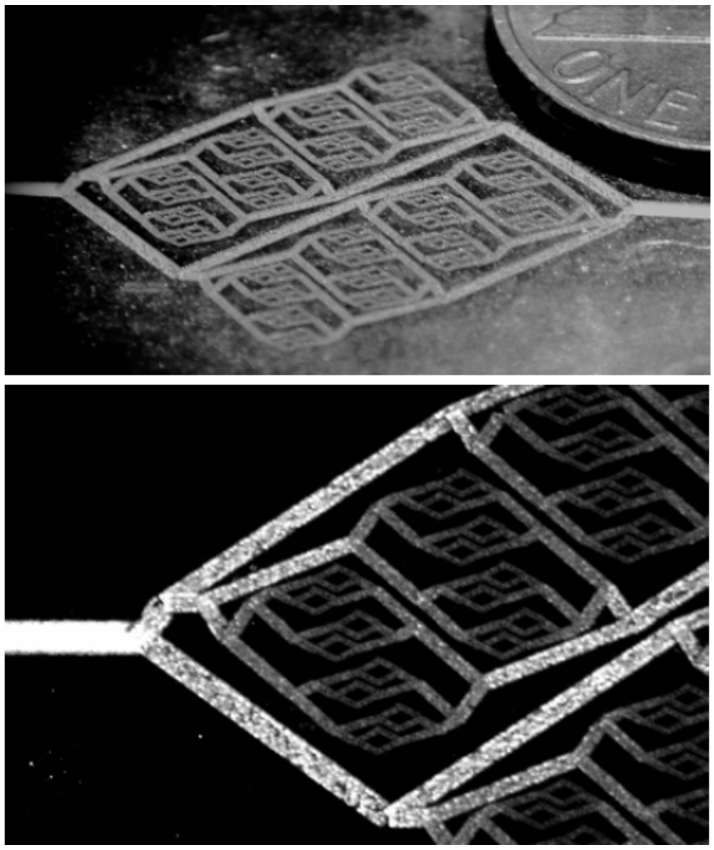

Figure 5.5: (Top) An eight level multi-width multi-level microvasculature network microchannels fabricated by one-step laser direct write. The dimensions for the various branch generations are $w_1=d_1=660$ µm, $w_2=d_2=525$ µm, $w_3=d_3=415$ µm, $w_4=d_4=330$ µm, $w_5=d_5=260$ µm $w_6=d_6=210$ µm $w_7=d_7=165$ µm and $w_8=d_8=130$ µm (Bottom) Image showing the difference in intensity levels corresponding to different channel's depth.

5.6 References

Abramowitz S. DNA Analysis in Microfabricated Formats. J. Biomed. Microdev., 1999; 1: 107-112.

Aunins JG, Bader B, Caola A, Griffiths J, Katz M, Licari P, Ram K, Ranucci CS, Zhou WC. Fluid mechanics, cell distribution, and environment in CellCube bioreactors. Biotechnol. Prog., 2003; 19: 2-8.

Bäuerle D. Laser Processing and Chemistry, 2nd ed., 1996; Springer: New York.

Beebe DJ, Mensing GA, Walker GM. Physics and applications of microfluidics in biology. Annu. Rev. Biomed. Eng., 2002; 4: 261-286.

Benavides SGL, Adams DP, Yang P. Meso-Machining Capabilities. Tech. Rep. SAND2001-1708, Sanida National Laboratories, AL, NM, 2001.

Bertsch A, Lorenz H, Renaud P. Sens. Actuators A. 3D microfabrication by combining microstereolithography and thick resist UV lithography 1999; 73: 14-23.

Bessoth FG, deMello AJ, Manz A. Microstructure for efficient continuous flow mixing. Anal. Commun., 1999; 36: 213-215.

Borenstein J, Terai H, King K, Weinberg E, Kaazempur-Mofrad M, Vacanti J. Microfabrication Technology for Vascularized Tissue Engineering. J. Biomed. Microdev., 2002; 4: 167-175.

Branebjerg J, Gravesen P, Krog JP, Nielsen CR. Fast mixing by lamination. Proc. IEEE Microelectromech. Syst. Workshop Dig., 1996; 441-446.

Chen C, Hirdes D, Folch A. Gray-scale photolithography using microfluidic photomasks. Proc. Natl. Acad. Sci. U. S. A, 2003;100: 1499-1504.

Chen ZP, Zhao YH, Srinivas SM, Nelson JS, Prakash N, Frostig RD. IEEE J SEL. TOP. QUANT., 1999; 5: 1134-1142.

Däschner W, Long P, Larsson M, Lee SH. Fabrication of diffractive optical elements using a single optical exposure with a gray level mask. J. Vac. Sci. Technol. B, 1995; 13: 2729-2731.

Dauer S, Ehlert A, Büttgenbach S. Micromechanical three-axial tactile force sensor for micromaterial characterization. Sens. Actuators A., 1999; 76: 381-385.

Dauer S. Ph.D thesis, 1999, Shaker Verlag.

Feldstein MJ, Golden JP, Rowe CA, MacCraith BD, Ligler FS. Array Biosensor: Optical and Fluidics Systems. J. Biomed. Microdev., 1999; 1: 139-153.

Gower M, Industrial applications of laser micromachining. Opt. Express, 2000; 7: 56-67.

Gray BL, Lieu DK, Collins SD, Smith RL, Barakat AI. Microchannel Platform for the Study of Endothelial Cell Shape and Function. J. Biomed. Microdev., 2002; 4: 9-16.

Harvey EC, Rumsby PT, Gower MC, Remnant JL. Microstructuring by excimer laser. SPIE Conf. on Micromachining and Microfabrication Process Tech., 1995; 2639: 266-277.

Hitt DL, Lowe ML. Confocal imaging of flows in artificial venular bifurcations. J. Biomech. Eng.-T ASME, 1999; 121: 170-177.

Johnson TJ, Ross D, Locascio LE. Rapid microfluidic mixing. Anal. Chem., 2002; 74: 45-51.

Klotzücher T, Gillner A. Handbuch Mikrotechnik (W. Ehrfeld, ed.), Munich: Hanser, 2002; 105-143.

Knowles M, Rutterford G, Bell A, Andrews A, Foster-Turner G, Kearsley A. Sub-micron and high precision micro-machining using nanosecond lasers. Laser Materials Processing 1998; 85: 112-120.

Koch M, Chatelain D, Evans AGR, Brunnschweiler A. Two simple micromixers based on silicon. J. Micromech. Microeng., 1998; 8: 123-126.

Legge CH. Chemistry under the Microscope—Lab-on-a-Chip Technologies. J. Chem. Educ., 2002; 79: 173-178.

Ma NN, Koelling KW, Chalmers JJ. Fabrication and use of a transient contractional flow device to quantify the sensitivity of mammalian and insect cells to hydrodynamic forces. Biotechnol. Bioeng., 2002; 80: 428-437.

Machan J, Valley M, Holleman G, Mitchell M, Burchman D, Zamel J, Harpole G, Injeyan H, Marabella L. Diode-pumped Nd:YAG laser for precision laser machining. J. Laser Appl., 1996; 8: 225-232.

Madou J. Fundamentals of Microfabrication: The Science of Miniaturization, 2nd ed., 2002; CRC Press: Boca Raton.

Murray C. The Physiological Principle of Minimum Work. I. The Vascular System and the Cost of Blood Volume. Proc. Nat. Acad. Sci. U.S.A., 1926; 12: 207-214.

Murray C, A relationship between circumference and weight in trees and its bearing on branching angles. J. Gen. Physiol., 1926; 9: 835-841.

Rizvi NH, Apte P. Developments in laser micro-machining techniques. J. Mat. Processing Tech. 2002; 127: 206-210.

Sampsell JB. Digital micromirror device and its application to projection displays. J. Vac. Sci. Technol. B, 1994; 12: 3242-3246.

Schwesinger N, Frank T, Wurmus H. A modular microfluid system with an integrated micromixer. J. Micromech. Microeng., 1996; 6: 99-102.

Shirk M, Molian P. A review of ultrashort pulsed laser ablation of materials. J. Laser Appl., 1998; 10: 18-28.

Stroock AD, Dertinger SKW, Ajdari A, Mezic I, Stone HA, Whitesides GM. Chaotic Mixer for Microchannels. Science, 2002; 295: 647-651.

Therriault D, White SR, Lewis JA. Chaotic mixing in three-dimensional microvascular networks fabricated by direct-write assembly. Nature Materials, 2003; 2: 265-271.

Wagner B, Quenzer HJ, Henke W, Hoppe W, Pilz W. Microfabrication of complex surface topographies using grey-tone lithography. Sens. Actuators A 1995; 46: 89-94.

Yoshimura Y, Hiramatsu Y, Sato Y, Homma S, Enomoto Y, Kikuchi Y, Sakakibara Y. Activated neutrophils and platelet microaggregates impede blood filterability through microchannels during simulated extracorporeal circulation. Ann. Thorac. Surg., 2003; 75: 1254-1260.

Chapter 6

Conclusions

Future Directions

Microsystem components integrated to create an artificial alveoli

The above chapters describe microsystems that allow us to recreate microenvironments to study cellular phenomena. Microtechnology provides us with the tools necessary to overcome the limitations of traditional bioassay systems with the advantage of smaller volumes, reduced reaction times, and the potential for integration. This thesis describes projects that use the advantages of microtechnology to probe cellular behavior. The cell stretching microwells can be potentially used to study the effects of cyclic stretch, not just on alignment, but also on other phenomena such as cell permeability, apoptosis, cytoskeletal rearrangements, changes in gene expression, or the release of cytokines. To study VILI, alveolar type I or type II cells can be cultured within the wells and exposed to physiologically relevant strains associated with MV and note their responses in regards to increased cellular death or the release of inflammatory cytokines such as IL-8. The air-liquid well system is a unique system capable of stretching cells in a physiologically relevant situation within alveoli. To measure the release of cytokines or other distress signals due to cyclic stretch, an on-chip nondiluting immunoassay such as the one described in chapter 4 is necessary. The microfluidic immunoassay system is amenable to studying not just IL-8, but also multiple cytokines

simultaneously as well as optimized for increased throughput and automation. The multigenerational branching network is an additional system that can be used to either supply nutrients and oxygen to the alveolar structures, or be cultured with cells that can release signals downstream to the alveolar epithelium. A complete system will allow us to study how alveolar cells sense mechanical stresses and respond to varying levels of stretch in the small volumes that recreate a physiological alveolar space.

Implications for VILI treatment

VILI is a significant health risk for patients who face mortality not only from ARDS, but also with the additional danger from mechanical ventilation. Current therapies seek to understand the ventilator settings required not only to sustain life, but to prevent this type of lung injury. Although great strides have been made in elucidating the mechanism underlying VILI, there is still a lot to be learned about the specific triggers for VILI and sustaining the inflammatory response. Once it is clear how mechanical ventilation effects these detrimental lung responses, steps can be taken to reduce the risk of VILI and develop effective, protective ventilation strategies in an already compromised and vulnerable lung. Therapies can focus not only on limiting the mechanical aspects of injury but also to constrain and modulate the inflammatory response.